

# Real-Space Methods for Ab Initio Modeling of Surfaces and Interfaces under External Potential Bias

Published as part of *Journal of Chemical Theory and Computation* special issue “Developments of Theoretical and Computational Chemistry Methods in Asia”.

Kartick Ramakrishnan, Gopalakrishnan Sai Gautam,\* and Phani Motamarri\*



Cite This: <https://doi.org/10.1021/acs.jctc.5c00513>



Read Online

ACCESS |

Metrics & More

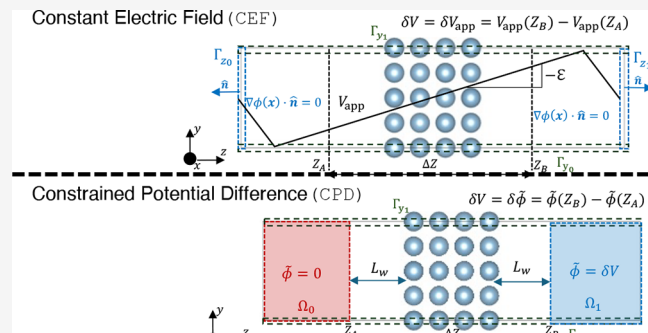
Article Recommendations

Supporting Information

**ABSTRACT:** Accurate ab initio modeling of surfaces and interfaces, especially under an applied external potential bias, is important for describing and characterizing various phenomena that occur in electronic, catalytic, and energy storage devices. Leveraging the ability of real-space density functional theory (DFT) codes to accommodate generic boundary conditions, we introduce two methods for applying an external potential bias that can be suitable for modeling surfaces and interfaces. In the first method, an external constant electric field is applied by modifying the DFT Hamiltonian via the introduction of an auxiliary linear potential while solving the electrostatic potential arising in DFT using a Poisson equation with zero-Neumann boundary conditions. The second method directly enforces the desired external potential bias by imposing constraints on the electrostatic potential, thereby naturally mimicking experimental conditions. We describe the underlying DFT governing equations for the two setups within the real-space formalism employing finite-element discretization. First, we validate the constant electric field setup within real-space finite-element DFT (DFT-FE) with an equivalent approach using plane-wave DFT (i.e., using periodic boundary conditions) on three representative benchmark systems, namely, La-terminated Li<sub>7</sub>La<sub>3</sub>Zr<sub>2</sub>O<sub>12</sub>, GaAs (111), and Al FCC (111) slabs. Subsequently, we present a comprehensive evaluation of the two setups in terms of the average ground-state properties, such as surface and adsorption energies. Also, we present an approach to constrain the electrostatic potential over a localised region, which is non-trivial to implement in periodic DFT codes. The methods developed in our work provide an attractive alternative to plane-wave DFT approaches in applying external potential bias that usually suffer from the periodic boundary conditions restrictions and poor scalability on parallel computing architectures. Our framework offers a robust approach for investigating surfaces and interfaces without any underlying assumptions or correction schemes while allowing for simulations of larger length scales than possible with plane-wave DFT.

## 1. INTRODUCTION

Ab initio calculations of surfaces and interfaces provide a rigorous, atomistic-level understanding of the intrinsic properties that govern their behavior in various applications. Accurate computation of surface energies, work functions, and the underlying ground-state electronic structures is critical for determining chemical reactivity, electronic phenomena, and catalytic adsorption. Typically, DFT simulations involving surfaces and interfaces are done using a 2-dimensional slab model of definite material thickness with a suitable vacuum layer employing periodic boundary conditions. This allows for detailed investigations into surface relaxation, surface reconstruction, defect formation, and diffusion mechanisms, which are pivotal in applications such as catalysis,<sup>1</sup> electronics,<sup>2</sup> energy storage,<sup>3,4</sup> and corrosion inhibition.<sup>5</sup>



Plane-wave density functional theory (PW-DFT) is a widely used approach today for accurate electronic structure calculations employing pseudopotentials. The popularity stems from the systematic convergence offered by the plane wave basis set, which ensures spectral convergence in the computation of ground-state material properties.<sup>6,7</sup> However, this choice of the basis set restricts the simulation domains to be periodic. Furthermore, sufficient vacuum sizes or large cell sizes are required to minimize the interaction between their

Received: April 1, 2025

Revised: June 2, 2025

Accepted: June 3, 2025

periodic images when computing ground state properties for molecules, nanoclusters, defective solids, slabs, and interfaces. Additionally, in the case of interfaces or surfaces with an intrinsic dipole moment, enforcing periodicity can lead to a spurious electric field, resulting in incorrect results and convergence issues.<sup>8</sup> To mitigate these effects, larger symmetric slabs can be employed to eliminate the net internal dipole moments. However, the requirement for large vacuums and larger slabs is computationally expensive, and the problem is compounded further by the inferior scaling of plane wave codes on modern supercomputing architectures.

To address the computational expense and convergence issues of surface/interface calculations, several strategies<sup>9,10</sup> have been proposed where an auxiliary linear potential is applied numerically to ensure the periodicity of electronic fields, often referred to as dipole correction schemes, which recover the original nature of the problem. Other approaches include incorporating Coulomb truncation kernels<sup>11,12</sup> which truncate the long-range Coulomb interactions between periodic images in plane-wave DFT codes. In contrast, real-space methods such as finite difference methods,<sup>13–17</sup> wavelet-based methods,<sup>18–20</sup> or finite-element (FE) methods<sup>21–36</sup> naturally accommodate generic boundary conditions and are systematically improvable while exhibiting excellent scalability on massively parallel computing architectures. In these methods, zero-Neumann boundary conditions on the electrostatic potential (i.e., the normal components of potential gradients are set to zero) can be imposed on the boundary parallel to the slab surface with an additional constraint imposed to fix the electrostatic potential reference. Notably, for neutral slabs, zero-Neumann boundary conditions can eliminate the need for dipole correction schemes and a large vacuum, improving accuracy and computational efficiency using real-space methods.

Beyond analyzing ground-state properties of material systems involving surfaces and interfaces, such as surface energies and work of adhesion, it is often necessary to investigate the other material parameters that control surface reactivity, diffusion mechanisms, and surface polarizability to understand key phenomena in various applications. Such important material properties or parameters can be tuned by applying an external potential bias across the slab, i.e., by applying an external electric field. For example, applying an external potential bias enables the tuning of surface polarization to control ferroelectricity in nanoscale electronics<sup>37</sup> and the manipulation of spin polarization for spintronic applications.<sup>38</sup> Additionally, external bias can regulate surface adsorption and modify chemical kinetics to enhance catalytic performance.<sup>39,40</sup> In battery systems, electrode/electrolyte interfaces experience significant electrostatic potential differences, which can alter ion migration pathways, ultimately impacting performance and efficiency.<sup>41,42</sup> Moreover, electrochemical impedance spectroscopy is a commonly used characterization technique in electrochemical devices that involves the application of an alternating potential bias across an interface to study the ionic and electronic transport mechanisms within the interface or material of interest.<sup>43</sup>

So far, PW-DFT calculations<sup>44–46</sup> have been used to provide theoretical insights into the effect of applying an external potential bias, where the bias is typically treated as a constant external electric field across the material system,<sup>44,47–49</sup> which may not depict what is actually happening in a system. An alternative approach, based on Green's functions,<sup>50</sup> reformu-

lates the electrostatic problem such that the computational domain is decoupled from periodic boundary conditions through an analytical form of Green's functions for Poisson's equation for various boundary conditions. However, this method is restricted to boundary conditions for which an explicit analytical form of Green's function is available. Thus, it is important to develop strategies to accurately model scenarios where an external potential bias is applied to a surface or an interface system, during either device operation or during characterization. In this work, we focus on developing real-space strategies for applying an external electrostatic potential bias at a fixed number of electrons and demonstrate on materials systems with no net electron transfer. Note that extensions of real-space frameworks that incorporate constant chemical potentials, allowing for the number of electrons to vary (i.e., grand canonical approaches<sup>51</sup>), are part of ongoing work.

Here, we leverage the ability of real-space density functional theory (DFT) methodologies to accommodate generic boundary conditions to introduce two setups for applying an external potential bias across a slab system: (a) imposing a uniform constant external electric field (CEF) and (b) directly applying a constrained potential difference (CPD). We introduce both setups using aperiodic boundary conditions in the DFT electrostatics problem. In the CEF setup, the external electric field is the tuning parameter that determines the resulting applied potential difference across the slab, as commonly done in plane-wave codes.<sup>44–46</sup> To achieve a CEF in real-space DFT, we need to impose a constant external electric field in the nonperiodic direction of the slab by modifying the DFT Hamiltonian, which is done by adding a sawtooth-shaped potential to the Kohn–Sham effective potential. Note that the linear segment of the sawtooth potential has a slope corresponding to the magnitude of the applied electric field. Further, the electrostatic problem involving the total charge density is solved by imposing zero-Neumann boundary conditions with a zero mean value constraint to fix the reference of the electrostatic potential. In the CPD setup, we directly control the electrostatic potential near the slab boundaries, providing a more natural representation of experimental setups in which an explicit potential bias is applied. In the CPD approach, the underlying electrostatic problem corresponding to the total charge density is solved by imposing inhomogeneous Dirichlet boundary conditions that respect the external potential bias, which ensures that the potential bias across the slab is maintained during the self-consistent field iteration employed for solving the underlying DFT problem. Further, we extend the CPD approach by localizing the region where the electrostatic potential is constrained (or the L-CPD approach), which cannot be trivially implemented in PW-DFT.

We have adopted a finite-element (FE) methodology for solving the DFT problem in our current work. FE basis sets are systematically convergent and compactly supported piecewise polynomial bases that can naturally accommodate generic boundary conditions. The locality of FE basis sets can exploit fine-grained parallelism on modern heterogeneous architectures while ensuring excellent scalability on distributed systems.<sup>52,53</sup> Indeed, recent studies<sup>35,36,53,54</sup> have demonstrated that FE-based methods significantly outperform plane-wave approaches for norm-conserving pseudopotential DFT calculations, particularly for large systems to achieve a given accuracy of ground-state energy and forces.<sup>33,55</sup> The open-

source code DFT-FE<sup>53,54</sup> incorporates these features while leveraging scalable and efficient solvers for solving the Kohn–Sham equations. Additionally, the recently developed projector augmented wave method formalism within the FE framework (PAW-FE)<sup>56</sup> has demonstrated nearly a 10-fold speedup over existing FE-based norm-conserving pseudopotential methods, thereby extending the length scales accessible to DFT computations. In this work, we implement both setups (CEF and CPD) for applying an external potential bias within the DFT-FE framework employing norm-conserving pseudopotentials, utilizing the advantages discussed earlier, thereby establishing a robust framework for large-scale simulations of surfaces and interfaces under an external potential bias and we note that extension to PAW-FE is straightforward.

We begin by benchmarking the CEF setup implemented in DFT-FE with an equivalent approach<sup>9,47</sup> used in plane wave codes. We consider three representative systems for our benchmarking, namely, La-terminated Li<sub>7</sub>La<sub>3</sub>Zr<sub>2</sub>O<sub>12</sub> (LLZO), GaAs(111), and Al FCC(111) slab, covering a diverse range of systems from polar to nonpolar and from insulating to metallic, with applications in semiconductor devices, solid-state batteries, and catalysis. Subsequently, to examine the differences between the two setups (CEF vs CPD) in DFT-FE, we plot the planar average electron density and planar average bare potential as a function of position along the nonperiodic direction for the benchmark systems considered. Importantly, we observe that the bare potential for a given material system at the ground state is different between the CEF and CPD, resulting in different ground-state solutions. Finally, we compare the surface energy of the (111) GaAs slab and La-terminated LLZO, and the adsorption energy of Na on the Al(111) surface as a function of the tuning parameters available in the CEF and CPD setups. Also, we extend a comparison of the surface energies and dipole moments in the GaAs (111) surface between the CPD and the L-CPD approaches.

The remainder of this article is structured as follows: Section 2 discusses the real-space formulation and FE discretization necessary for solving the Kohn–Sham ground-state problem. A detailed description of the two methods (and extension to L-CPD) of applying an external potential bias is presented. Section 3 presents a comprehensive benchmarking of the CEF setup against an equivalent approach used in plane-wave codes. Following this, we demonstrate the differences between CEF and CPD setups in DFT-FE when applying an external potential bias across the slab and extend the comparison by evaluating the surface energy of GaAs(111) and La-terminated LLZO, as well as the adsorption energy of Na on Al(111). Finally, we discuss our observations, outline future prospects arising from this work, and finish with a few concluding remarks.

## 2. METHODS

In this section, we outline the governing equations for determining the ground-state material properties involving slab models within the real-space formalism employed in this work. Subsequently, we examine different approaches for incorporating an external potential bias, detailing the modifications to the Hamiltonian and the resulting energy and ionic forces expressions. Finally, we provide an overview of the FE formulation used in this work to compute the ground-state properties of slabs under an applied potential bias.

### 2.1. Governing Equations and Force Expression in DFT-FE.

The ground-state properties of a slab comprising  $N_a$  nuclei and  $N_e$  electrons in a representative supercell within the norm-conserving pseudopotential formalism are governed by the following Kohn–Sham density functional theory (DFT) energy functional<sup>57,58</sup>:

$$E[\{\psi_n\}, \{\mathbf{R}^a\}] = \min_{\{\psi_n\} \in \chi(\Omega_p)} \{T_s + E_{xc} + E_{el} + E_{psp}\} \quad (1)$$

where  $\{\psi_n\}$  denotes the single-electron wave functions satisfying the orthonormality condition  $\langle \psi_i | \psi_j \rangle = \delta_{ij}$  with  $1 \leq n \leq N$  where  $N \geq \frac{N_e}{2}$ , and  $\{\mathbf{R}^a\}$  signifies the position vectors of the  $N_a$  nuclei. We note that  $\chi(\Omega_p)$  denotes an appropriate function space in which the single-electron wave functions lie, with  $\Omega_p$  representing the 2D periodic slab domain. We focus here on the spin-unpolarized DFT formulation for clarity and notational convenience, while the extension to the spin-polarized framework is straightforward.

The term  $T_s$  in eq 1 represents the kinetic energy of the noninteracting electrons, while  $E_{xc}$  represents the exchange-correlation energy that accounts for the quantum mechanical many-body effects, and is given by

$$\begin{aligned} T_s[\{\psi_n\}] &= 2 \sum_n f_n \int \frac{1}{2} |\nabla \psi_n(\mathbf{x})|^2 d\mathbf{x}, \\ E_{xc}[\rho(\mathbf{x})] &= \int \epsilon_{xc}[\rho(\mathbf{x}), \nabla \rho(\mathbf{x})] d\mathbf{x} \end{aligned} \quad (2)$$

where the generalized gradient approximation<sup>58–60</sup> (GGA) has been adopted for the exchange-correlation contribution. Further, the electron density ( $\rho(\mathbf{x})$ ) and its gradient ( $\nabla \rho(\mathbf{x})$ ) in eq 2 are computed as,

$$\begin{aligned} \rho(\mathbf{x}) &= 2 \sum_n f_n |\psi_n(\mathbf{x})|^2; \\ \nabla \rho(\mathbf{x}) &= 2 \sum_n f_n (\psi_n^*(\mathbf{x}) \nabla \psi_n(\mathbf{x}) + \psi_n(\mathbf{x}) \nabla \psi_n^*(\mathbf{x})) \end{aligned} \quad (3)$$

with  $\mathbf{x}$  denoting the spatial coordinate, and  $f_n$  is the occupation number corresponding to the electronic wave function indexed by ‘ $n$ ’ in the above. Furthermore,  $E_{el}$  in eq 1 represents the classical electrostatic energy computed as

$$\begin{aligned} E_{el}[\rho(\mathbf{x}), \{\mathbf{R}^a\}] &= \max_{\hat{\phi} \in \kappa(\Omega_p)} \left\{ \int_{\Omega_p} (\rho(\mathbf{x}) + b(\mathbf{x})) \hat{\phi}(\mathbf{x}) d\mathbf{x} \right. \\ &\quad \left. - \frac{1}{8\pi} \int_{\Omega_p} |\nabla \hat{\phi}(\mathbf{x})|^2 d\mathbf{x} \right\} - \sum_a E_{self}^a \end{aligned} \quad (4)$$

where  $\hat{\phi}(\mathbf{x})$  denotes the trial function for the electrostatic potential due to the total charge density ( $\rho(\mathbf{x}) + b(\mathbf{x})$ ) and belongs to a suitable function space  $\kappa(\Omega_p)$ . Additionally,  $E_{self}^a$  in eq 4 represents the self-energy associated with an atom-centered smeared charge density  $b_{sm}^a(\mathbf{x})$ .  $E_{self}^a$  arises from introducing the atom-centered smeared charges in the local real-space electrostatics reformulation, which leads to an additional atom-centered potential,  $V_{sm}^a(\mathbf{x} - \mathbf{R}^a)$  (see eq 17 in our previous work<sup>54</sup>). Moreover, the electrostatic potential  $\phi(\mathbf{x})$  generated by the total charge density ( $\rho(\mathbf{x}) + b(\mathbf{x})$ ), where  $b(\mathbf{x}) = \sum_a b_{sm}^a(\mathbf{x} - \mathbf{R}^a)$ , is obtained by solving the following Poisson’s equation,

$$-\frac{1}{4\pi}\nabla^2\phi(\mathbf{x}) = \rho(\mathbf{x}) + b(\mathbf{x}) \quad (5)$$

that corresponds to the Euler–Lagrange equation associated with the maximization problem in eq 4. Finally,  $E_{\text{psp}}[\{\psi_n\}, \{\mathbf{R}^a\}]$  in eq 1 represents the pseudopotential energy contribution, which is written as the sum of local and nonlocal contributions, i.e.,  $E_{\text{psp}}[\{\psi_n\}, \{\mathbf{R}^a\}] = E_{\text{loc}}[\rho(\mathbf{x})] + E_{\text{nloc}}[\{\psi_n\}, \{\mathbf{R}^a\}]$ , where the local pseudopotential,  $E_{\text{loc}}$ , is expressed as

$$E_{\text{loc}}[\rho(\mathbf{x})] = \int_{\Omega_p} (V_{\text{loc}}(\mathbf{x}) - V_{\text{sm}}(\mathbf{x}))\rho(\mathbf{x})d\mathbf{x} \quad (6)$$

In the above equation,  $V_{\text{loc}}(\mathbf{x})$  is the sum of atom-dependent local pseudopotentials, i.e.,  $V_{\text{loc}}(\mathbf{x}) = \sum_a V_{\text{loc}}^a(\mathbf{x} - \mathbf{R}^a)$ , while  $V_{\text{sm}}(\mathbf{x}) = \sum_a V_{\text{sm}}^a(\mathbf{x} - \mathbf{R}^a)$ . Since the electrostatic energy computed from eq 4 involves the electrostatic potential  $\phi(\mathbf{x})$  due to the electron charge and smeared charge density, i.e.,  $\rho(\mathbf{x}) + b(\mathbf{x})$ , the energy contribution given by  $E_{\text{loc}}[\rho(\mathbf{x})]$  term not only includes the contribution from  $V_{\text{loc}}(\mathbf{x})$  but is adjusted to exclude the contribution of  $V_{\text{sm}}(\mathbf{x})$  arising from the smeared charge density  $b(\mathbf{x})$ . Additionally, the nonlocal pseudopotential energy contribution,  $E_{\text{nloc}}$ , for optimized norm-conserving (or ONCV) pseudopotentials<sup>61</sup> is given by

$$E_{\text{nloc}}[\{\psi_n\}, \{\mathbf{R}^a\}] = 2 \sum_n f_n \int_{\Omega_p} \int \psi_n^*(\mathbf{x}) V_{\text{nloc}}(\mathbf{x}, \mathbf{y}) \psi_n(\mathbf{y}) d\mathbf{y} d\mathbf{x} \quad (7)$$

where the action of  $V_{\text{nloc}}(\mathbf{x}, \mathbf{y})$  on electronic wave function is given by

$$\begin{aligned} & \int V_{\text{nloc}}(\mathbf{x}, \mathbf{y}) \psi_n(\mathbf{y}) d\mathbf{y} \\ &:= \sum_a \sum_\beta p_\beta^a(\mathbf{x} - \mathbf{R}^a) D_\beta^a \int p_\beta^a(\mathbf{y} - \mathbf{R}^a) \psi_n(\mathbf{y}) d\mathbf{y} \end{aligned} \quad (8)$$

The composite index  $\beta = \{n, l, m\}$  in eq 8 is such that  $l$  and  $m$  denote the orbital and magnetic angular momentum indices, respectively. Furthermore,  $p_\beta^a(\mathbf{x} - \mathbf{R}^a)$  indicates the atom-centered projector of index  $\beta$ , while  $D_\beta^a$  represents the pseudopotential coupling coefficients. Finally, the problem of determining the ground-state properties for given positions of nuclei ( $\{\mathbf{R}^a\}$ ) is determined by solving the following variational problem,

$$\begin{aligned} E_{\text{GS}}[\{\psi_n\}, \{\mathbf{R}^a\}] = & \min_{\{\psi_n\} \in \chi(\Omega_p)} \max_{\hat{\phi} \in \kappa(\Omega_p)} \left\{ T_s[\{\psi_n\}] \right. \\ & - \frac{1}{8\pi} \int_{\Omega_p} |\nabla \hat{\phi}(\mathbf{x})|^2 d\mathbf{x} + \int_{\Omega_p} (\rho(\mathbf{x}) + b(\mathbf{x})) \hat{\phi}(\mathbf{x}) d\mathbf{x} \\ & \left. - \sum_a E_{\text{self}}^a + E_{\text{xc}}[\rho(\mathbf{x})] + E_{\text{loc}}[\rho(\mathbf{x})] + E_{\text{nloc}}[\{\psi_n\}, \{\mathbf{R}^a\}] \right\} \end{aligned} \quad (9)$$

The Euler–Lagrange equation corresponding to the minimization of the energy functional in eq 9 subject to the orthonormality constraint on the single-electron wave functions ( $\int \psi_i^*(\mathbf{x}) \psi_j(\mathbf{x}) d\mathbf{x} = \delta_{ij}$ ), leads to the Hermitian eigenvalue problem  $\mathcal{H}\psi_i = \epsilon_i \psi_i$  that needs to be solved for the smallest  $N \geq N_e/2$  eigenpairs  $\{\epsilon_i, \psi_i\}$  of the Hamiltonian operator  $\mathcal{H}$ . In turn,  $\mathcal{H}$  is decomposed as  $\mathcal{H} = \mathcal{H}_{\text{loc}} + \mathcal{H}_{\text{nloc}}$ , where  $\mathcal{H}_{\text{loc}}$  is defined to be,

$$\mathcal{H}_{\text{loc}} = \left[ -\frac{1}{2}\nabla^2 + V_{\text{eff}}(\mathbf{x}) \right], \text{ with}$$

$$V_{\text{eff}}(\mathbf{x}) := \left( \frac{\delta E_{\text{xc}}}{\delta \rho(\mathbf{x})} [\rho(\mathbf{x}), \nabla \rho(\mathbf{x})] + \tilde{\phi}(\mathbf{x}) \right) \quad (10)$$

with  $\tilde{\phi}(\mathbf{x}) := \phi(\mathbf{x}) + V_{\text{loc}}(\mathbf{x}) - V_{\text{sm}}(\mathbf{x})$ , henceforth referred to as the total electrostatic potential, which includes the electron–electron and electron–nuclear interactions. Additionally, the action of  $\mathcal{H}_{\text{nloc}}$  on wave function  $\psi_n(\mathbf{x})$  is defined as

$$\mathcal{H}_{\text{nloc}}\psi_n := \sum_a^{N^a} \int V_{\text{nloc}}^a(\mathbf{x}, \mathbf{y}) \psi_n(\mathbf{y}) d\mathbf{y} \quad (11)$$

When dealing with periodic crystals, 2D slabs or surfaces, it is computationally efficient to invoke Bloch's theorem<sup>58,62</sup> along the periodic directions, and instead of solving the problem on large periodic supercells, we solve the problem on smaller unit cells with periodic boundary conditions. Using Bloch's theorem, the electronic wave function can be expressed as  $\psi_{nk}(\mathbf{x}) = e^{ik \cdot \mathbf{x}} u_{nk}(\mathbf{x})$ , where  $i = \sqrt{-1}$  and  $u_{nk}(\mathbf{x})$  is a lattice-periodic function satisfying  $u_{nk}(\mathbf{x} + \mathbf{L}_r) = u_{nk}(\mathbf{x})$  for all reciprocal lattice vectors  $\mathbf{k}$  in the first Brillouin zone and for all lattice vectors  $\mathbf{L}_r$  in the periodic directions. To this end, the governing equations involving Bloch wave functions to be solved for determining the ground-state properties are given as follows:

$$\begin{aligned} \mathcal{H}^k u_{nk} &= \epsilon_{nk} u_{nk} \quad \text{with} \quad \mathcal{H}^k := \mathcal{H}_{\text{loc}}^k + \mathcal{H}_{\text{nloc}}^k \\ -\frac{1}{4\pi} \nabla^2 V_{\text{sm}}^a &= b_{\text{sm}}^a(\mathbf{x} - \mathbf{R}^a), \quad -\frac{1}{4\pi} \nabla^2 \phi(\mathbf{x}) = \rho(\mathbf{x}) + b(\mathbf{x}) \end{aligned} \quad (12)$$

where  $\mathcal{H}_{\text{loc}}^k$  and the action of  $\mathcal{H}_{\text{nloc}}^k$  on a wave function are given by eq 13

$$\begin{aligned} \mathcal{H}_{\text{loc}}^k &:= \left[ -\frac{1}{2}\nabla^2 - ik \cdot \nabla + \frac{1}{2}|\mathbf{k}|^2 + V_{\text{eff}}(\mathbf{x}) \right], \\ V_{\text{eff}}(\mathbf{x}) &:= \left[ \frac{\delta E_{\text{xc}}[\rho(\mathbf{x}), \nabla \rho(\mathbf{x})]}{\delta \rho(\mathbf{x})} + \tilde{\phi}(\mathbf{x}) \right] \\ \tilde{\phi}(\mathbf{x}) &= \phi(\mathbf{x}) + (V_{\text{loc}}(\mathbf{x}) - V_{\text{sm}}(\mathbf{x})) \\ V_{\text{loc}}(\mathbf{x}) &= \sum_r \sum_{a \in \Omega_p} V_{\text{loc}}^a(\mathbf{x} - \mathbf{R}^a + \mathbf{L}_r), \\ V_{\text{sm}}(\mathbf{x}) &= \sum_r \sum_{a \in \Omega_p} V_{\text{sm}}^a(\mathbf{x} - \mathbf{R}^a + \mathbf{L}_r) \\ \rho(\mathbf{x}) &= 2 \sum_n \int_{BZ} f_{nk} |u_{nk}(\mathbf{x})|^2 d\mathbf{k}, \\ \nabla \rho(\mathbf{x}) &= 2 \sum_n \int_{BZ} f_{nk} (u_{nk}^*(\mathbf{x}) \nabla u_{nk}(\mathbf{x}) + u_{nk}(\mathbf{x}) \nabla u_{nk}^*(\mathbf{x})) d\mathbf{k} \\ \mathcal{H}_{\text{nloc}}^k u_{nk} &:= \sum_{a \in \Omega_p} \left[ \sum_\beta \left\{ \sum_r e^{-ik \cdot (\mathbf{x} - \mathbf{L}_r)} p_\beta^a(\mathbf{x} - \mathbf{R}^a - \mathbf{L}_r) \right\} \right. \\ &\quad \left. D_\beta^a \left( \int_{\Omega_p} \sum_{r'} e^{ik \cdot (\mathbf{y} - \mathbf{L}_{r'})} p_\beta^a(\mathbf{y} - \mathbf{R}^a - \mathbf{L}_{r'}) u_{nk}(\mathbf{y}) d\mathbf{y} \right) \right] \end{aligned} \quad (13)$$

where  $f_{BZ}$  denotes the volume average of the integral over the first Brillouin zone (BZ) corresponding to the unit cell  $\Omega_p$ . A detailed discussion on computing ion forces and cell stresses can be found in our previous work.<sup>54,63</sup> For the sake of completeness, we mention here the expressions for the ionic force in the norm-conserving pseudopotential formulation:

$$\begin{aligned} F^a &= -\frac{dE_{GS}}{dR^a} = F_{loc}^a + F_{nloc}^a + F_{nloc}^{a*} \quad (14) \\ F_{loc}^a &= -\int_{\Omega_p} \nabla \rho(\mathbf{x}) (V_{loc}^a(\mathbf{x} - \mathbf{R}^a) - V_{sm}^a(\mathbf{x} - \mathbf{R}^a)) \\ d\mathbf{x} - \frac{1}{2} \int_{\Omega_p} b_{sm}^a(\mathbf{x} - \mathbf{R}^a) \nabla \phi(\mathbf{x}) d\mathbf{x} \end{aligned} \quad (14)$$

$$F_{nloc}^a = 2 \sum_{n=1}^N \int_{BZ} f_{n,k} \left[ \int_{\Omega_p} \sum_{\beta} \sum_r e^{-ik \cdot (\mathbf{x} - \mathbf{L}_r)} p_{\beta}^a(\mathbf{x} - \mathbf{R}^a - \mathbf{L}_r) d\mathbf{x} \right. \\ \left. D_{\beta}^a \int_{\Omega_p} \sum_{r'} e^{ik \cdot (\mathbf{y} - \mathbf{L}_{r'})} p_{\beta}^a(\mathbf{y} - \mathbf{R}^a - \mathbf{L}_{r'}) (-\nabla u_{nk}(\mathbf{y}) + ik u_{nk}(\mathbf{y})) d\mathbf{y} \right] dk$$

**2.2. Applying an External Potential Bias.** First, we consider the effect of a constant external electric field (or CEF), which is analogous to the sawtooth method with dipole correction employed in plane-wave codes.<sup>9,47</sup> Second, we examine the case where the classical electrostatic potential ( $\phi(\mathbf{x})$ ) conforms to the external potential bias through the boundary conditions imposed on  $\phi(\mathbf{x})$  in the Poisson equation (eq 5), termed the constrained potential difference (or CPD) setup.

**2.2.1. CEF Setup.** The typical approach to imposing an external electric field on slabs is to employ a sawtooth potential,<sup>47</sup> which is the method of choice for slabs in Quantum Espresso (QE)<sup>64</sup> and one of the approaches used in our work as well. An alternative approach to applying a constant electric field is by introducing a dipole sheet in the vacuum region.<sup>10,44</sup> In the current CEF setup, the effective potential ( $V_{eff}(\mathbf{x})$ ) in eq 10 is modified to take the form,

$$V_{eff}(\mathbf{x}) = \left( \frac{\delta E_{xc}}{\delta \rho(\mathbf{x})} [\rho(\mathbf{x}), \nabla \rho(\mathbf{x})] + \tilde{\phi}(\mathbf{x}) + V_{app}(\mathbf{x}) \right) \quad (15)$$

where  $V_{app}(\mathbf{x})$  is the linear periodic potential across the material system as indicated in Figure 1. The slope of  $V_{app}$

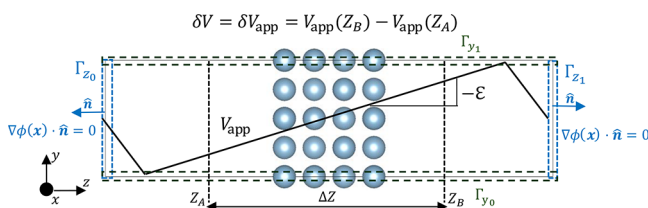


**Figure 1.** CEF: The boundary conditions for the electrostatic potential ( $\phi(\mathbf{x})$ ) are periodic along the  $x$  and  $y$  directions.  $\Gamma_{y_0}$ ,  $\Gamma_{y_1}$ ,  $\Gamma_{x_0}$  (not shown), and  $\Gamma_{x_1}$  (not shown) denote the periodic boundaries. Zero-Neumann conditions are applied on the nonperiodic boundaries  $\Gamma_{z_0}$ ,  $\Gamma_{z_1}$ . The constant electric field is applied by introducing the sawtooth potential  $V_{app}$ . The electric field ( $E$ ) is determined as  $-E\Delta Z = \delta V$ .

dictates the magnitude of the electric field,  $-E = \frac{dV_{app}}{dz}$  and ensures a straightforward benchmarking with plane-wave codes. We design the profile of  $V_{app}(\mathbf{x})$  to be a sawtooth function, similar to plane-wave codes, with the maximum and the minimum values located close to the simulation cell boundaries, as shown in Figure 1. Additionally, the sawtooth form acts as a constraining potential, preventing electron density leakage into the low-potential regions, allowing for better self-consistent field convergence, especially at higher

magnitudes of  $\mathcal{E}$ . Unlike the plane-wave basis, the electrostatic potential ( $\phi(\mathbf{x})$ ) in DFT-FE need not be fully periodic, and we impose semiperiodic boundary conditions on  $\phi(\mathbf{x})$  to simulate neutral slabs. Specifically, as displayed in Figure 1, we impose periodic boundary conditions in the  $x$ ,  $y$ -planar directions and a zero-Neumann boundary condition on the boundaries parallel to the slab surface while solving for  $\phi(\mathbf{x})$  using the Poisson equation (see eq 5). Additionally, we apply a zero mean-value constraint,  $\int_{\Omega_p} \phi(\mathbf{x}) d\mathbf{x} = 0$ , to fix the reference potential and remove the arbitrary constant offset.

Finally, we summarize the governing equation and boundary conditions to determine  $\phi(\mathbf{x})$  in the CEF setup as

$$\begin{cases} -\frac{1}{4\pi} \nabla^2 \phi(\mathbf{x}) = \rho(\mathbf{x}) + b(\mathbf{x}), \mathbf{x} \in \Omega_p \\ \phi(\mathbf{x})|_{\Gamma_{x_0}} = \phi(\mathbf{x})|_{\Gamma_{x_1}}, \phi(\mathbf{x})|_{\Gamma_{y_0}} = \phi(\mathbf{x})|_{\Gamma_{y_1}} \\ \nabla \phi(\mathbf{x}) \cdot \hat{n}|_{\Gamma_{z_0}} = 0, \nabla \phi(\mathbf{x}) \cdot \hat{n}|_{\Gamma_{z_1}} = 0, \int_{\Omega_p} \phi(\mathbf{x}) d\mathbf{x} = 0 \end{cases} \quad (16)$$

The inclusion of  $V_{app}(\mathbf{x})$  requires the energy functional in eq 9 to be modified as

$$E_{GS}[\{\psi_n\}, \{R^a\}] = \min_{\{\psi_n\} \in \phi} \max_{\{R^a\}} \left\{ T_s[\{\psi_n\}] - \frac{1}{8\pi} \int_{\Omega_p} |\nabla \phi(\mathbf{x})|^2 d\mathbf{x} \right. \\ \left. + \int_{\Omega_p} (\rho(\mathbf{x}) + b(\mathbf{x})) \phi(\mathbf{x}) d\mathbf{x} + \int_{\Omega_p} (\rho(\mathbf{x}) + b(\mathbf{x})) V_{app}(\mathbf{x}) d\mathbf{x} \right. \\ \left. + E_{xc}[\rho(\mathbf{x})] + E_{loc}[\rho(\mathbf{x})] + E_{nloc}[\{\psi_n\}, \{R^a\}] \right\} \quad (17)$$

Additionally, the ionic forces are modified as

$$F^a = F_{loc}^a + F_{nloc}^a + F_{nloc}^{a*} + F_{app}^a \quad (18)$$

where  $F_{loc}^a$ ,  $F_{nloc}^a$  are defined in eq 14,  $*$  denotes the complex conjugate and  $F_{app}^a = -\nabla V_{app} Z_v$ , with  $Z_v$  denoting the valence charge of atom "a".

**2.2.2. CPD Setup.** The natural approach to applying an external potential bias is to impose constraints on the total electrostatic potential ( $\tilde{\phi}(\mathbf{x})$ ) so that the desired potential difference is maintained. In contrast to the CEF setup, where  $\delta V_{app}$  is controlled via the value of the constant electric field, this method directly enforces the total electrostatic potential difference across the slab,  $\delta\tilde{\phi}$ , as the boundary condition. Since  $\delta\tilde{\phi}$  corresponds directly to the controlling parameters used in electrochemical and surface science measurements, this approach provides a more direct link to the experimental setup.

To implement CPD, the solution of the electrostatic variational problem in eq 4 should satisfy the boundary conditions shown in Figure 2. Furthermore, the CPD can be modified to localize the  $\Omega_1$  region as shown in the top panel of Figure 3, which we refer to as the locally constrained potential difference (L-CPD) setup. The bottom panel of Figure 3 highlights the difference in the  $\Omega_1$  region between the two setups. Finally, we can summarize the governing equation and boundary conditions for computing the electrostatic potential ( $\phi(\mathbf{x})$ ) in the CPD and the L-CPD setup as

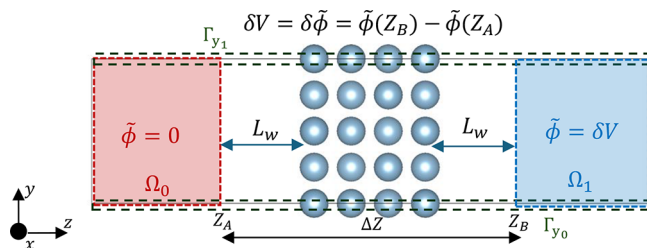


**Figure 2.** CPD: The boundary conditions for the total electrostatic potential ( $\tilde{\phi}(\mathbf{x})$ ) is periodic along the  $x$  and  $y$  directions.  $\Gamma_{y_0}$ ,  $\Gamma_{y_1}$  (not shown), and  $\Gamma_{x_1}$  (not shown) denote the periodic boundaries.  $Z_A$  and  $Z_B$  denote the interface between the vacuum and metal conductors.  $L_w$  denotes the distance between the surface and the metal conductors. Furthermore,  $\tilde{\phi}(\mathbf{x})$  is constrained in the region of metal conductors, as shown in the shaded region, ensuring the electric field in the conductor region is zero.

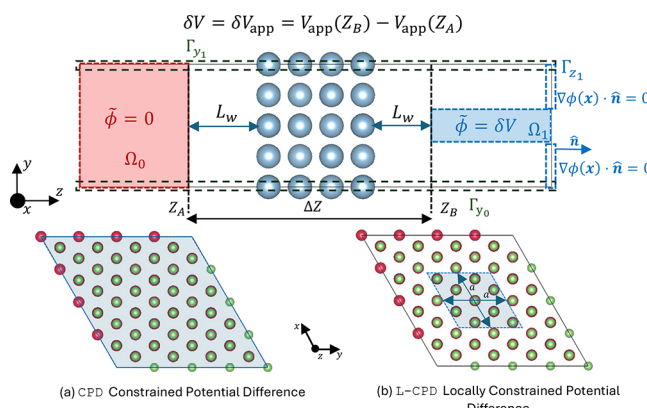


**Figure 3.** Top panel: L-CPD: The boundary conditions for the total electrostatic potential ( $\tilde{\phi}(\mathbf{x})$ ) is periodic along the periodic boundaries  $\Gamma_{y_0}$ ,  $\Gamma_{y_1}$ ,  $\Gamma_{x_0}$  (not shown), and  $\Gamma_{x_1}$  (not shown).  $Z_A$  and  $Z_B$  denote the interface between the vacuum and metal conductors.  $L_w$  denotes the distance between the surface and metal conductors.  $\tilde{\phi}(\mathbf{x})$  is constrained in the region of metal conductors, as shown in the shaded region, ensuring the electric field in the conductor is zero. Bottom panel: Comparison of (a) CPD and (b) L-CPD setups when viewed along the  $z$  axis for GaAs (Ga: red; As: green). The region in blue depicts the region on the surface where  $\tilde{\phi}$  is constrained to be  $V_{app}$ . ‘ $a$ ’ indicates the length scale of the region where  $\tilde{\phi}$  is applied in the L-CPD setup.

$$\begin{cases} -\frac{1}{4\pi}\nabla^2\phi(\mathbf{x}) = \rho(\mathbf{x}) + b(\mathbf{x}), \mathbf{x} \in \Omega_p \\ \phi(\mathbf{x})|_{\Gamma_{x_0}} = \phi(\mathbf{x})|_{\Gamma_{x_1}}, \phi(\mathbf{x})|_{\Gamma_{y_0}} = \phi(\mathbf{x})|_{\Gamma_{y_1}} \\ \phi(\mathbf{x}) = -(V_{loc}(\mathbf{x}) - V_{sm}(\mathbf{x})) \forall \mathbf{x} \in \Omega_0 \\ \phi(\mathbf{x}) = \delta V - (V_{loc}(\mathbf{x}) - V_{sm}(\mathbf{x})) \forall \mathbf{x} \in \Omega_1 \end{cases} \quad (19)$$

Notably, the Kohn–Sham energy functional remains unchanged from eq 9, thereby the governing equation and the expression for ionic forces are exactly the same as in eqs 12 and 14, respectively. We note that the electrostatic screening method,<sup>50</sup> designed for use with plane-wave codes, is in a similar spirit. However, it relies on Green’s functions of the Poisson equation for various boundary conditions, restricting

the applicability to only those cases where analytical solutions are available.

**2.3. FE Discretization.** We discretize the governing equation in eq 12 by employing the FE basis,<sup>65,66</sup> which comprises  $C^0$ -continuous piecewise Lagrange polynomials interpolated over Gauss–Lobatto–Legendre nodal points. To this end, the FE representation of the various electronic fields in eq 12 are given by,

$$u_{nk}^h(\mathbf{x}) = \sum_I^M N_I^{h,p}(\mathbf{x}) u_{nk}^I, \phi^h(\mathbf{x}) = \sum_I^M N_I^{h,p_{el}}(\mathbf{x}) \phi^I \quad (20)$$

where  $u_{nk}^I$ ,  $\phi^I$  represent the FE discretized fields, while  $N_I^{h,p}(\mathbf{x})$ ,  $N_I^{h,p_{el}}(\mathbf{x})$  are the strictly local Lagrange polynomials of degrees  $p$ ,  $p_{el}$ , respectively. The resulting discretized eigenvalue problem  $\mathbf{H}^k u_{nk} = \varepsilon_{n,k}^h \mathbf{M} u_{nk}$  is a nonlinear generalized eigenvalue problem where  $\mathbf{H}^k$  is the FE-discretized Hamiltonian and  $\mathbf{M}$  represents the FE-basis overlap matrix. Furthermore, to determine the electrostatic potential ( $\phi^h(\mathbf{x})$ ), the FE-discretized Poisson equation  $\mathbf{K}\phi = \mathbf{c}$  is solved with appropriate boundary conditions, where the entries of  $\mathbf{K}$  are  $K_{IJ} = \int_{\Omega_p} \nabla N_I^{h,p_{el}}(\mathbf{x}) \cdot \nabla N_J^{h,p_{el}}(\mathbf{x}) d\mathbf{x}$  and  $c_I = \int_{\Omega_p} N_I^{h,p_{el}}(\mathbf{x}) (\rho(\mathbf{x}) + b(\mathbf{x})) d\mathbf{x}$ . A detailed discussion on the eigensolver, self-consistent-field iteration related mixing strategies, and the efficient solution strategies that leverage the sparsity of the FE basis are discussed in our previous works.<sup>35,53,54,67</sup>

**2.4. Computational Details.** The two setups for applying an external potential bias (CEF and CPD), as discussed in the previous subsections, were implemented within the DFT-FE framework employing norm-conserving pseudopotentials. In our calculations, we employed GGA<sup>59,60</sup> for the exchange-correlation functional, specifically utilizing the Perdew–Burke–Ernzerhof (PBE) form,<sup>60</sup> as implemented in the libxc<sup>68</sup> library. Furthermore, the plane-wave calculations for some of the validation studies were performed using QE, using the dipfield option to enable dipole correction and the tefield option to add the sawtooth potential. The ONCV pseudopotentials<sup>61</sup> used for these simulations were from the pseudodojo<sup>69</sup> and SPMS<sup>70</sup> repositories (refer to Supporting Information, Section S1 for more details). The plane-wave discretization parameter,  $E_{cut}$  for QE, was selected such that the discretization error with respect to a refined calculation ( $E_{cut} = 100 E_h$ ) is of  $O(10^{-5}) \frac{E_h}{atom}$  for DFT ground-state energy,  $O(10^{-5}) \frac{E_h}{bohr}$  for ionic forces and  $O(10^{-6}) \frac{E_h}{bohr^3}$  for unit-cell stresses, wherever applicable. Similarly, the discretization parameters in DFT-FE are the FE interpolating polynomial degree ‘ $p$ ’ and mesh size around the atom ‘ $h$ ’. These were chosen such that a discretization error of  $O(10^{-5}) \frac{E_h}{atom}$  for ground-state energy,  $O(10^{-5}) \frac{E_h}{bohr}$  for ionic forces and  $O(10^{-6}) \frac{E_h}{bohr^3}$  was achieved with reference to a refined calculation ( $E_{cut} = 100 E_h$ ) in QE for each bulk system. For the Brillouin zone integration, we employ Monkhorst–Pack (MP) grids<sup>71</sup> to ensure systematic convergence of electronic properties. The  $k$ -point sampling rule for Brillouin zone integration was chosen so that the errors from successive refined samplings are higher order relative to the discretization errors incurred, ensuring the systematic convergence of electronic properties.

### 3. RESULTS

In this section, we begin by benchmarking the CEF setup implemented in DFT-FE against an equivalent setup<sup>9,47</sup> in QE. We compare the dipole moment, free energy, and ionic forces with various magnitudes of constant external electric fields and compute the dielectric response of the three systems considered in this work. Following this validation study for the CEF setup, we compare the CEF and the CPD setups by analyzing the difference in the ground state solutions of electron density ( $\rho(\mathbf{x})$ ) and bare potential ( $V_{\text{bare}}(\mathbf{x})$ ). Finally, we compare the influence of external potential bias in the two setups on ground-state properties, namely, surface and adsorption energies.

The systems considered in this work, as showcased in Figure 4, are (a) La-terminated LLZO slab, identified as one of the

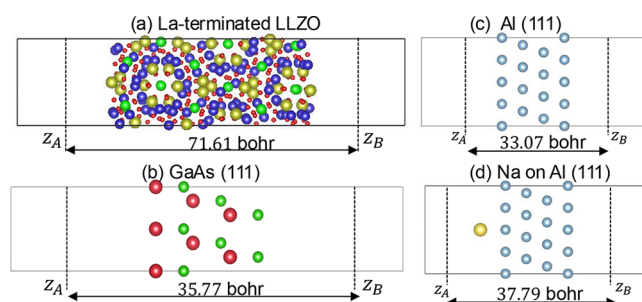


**Figure 4.** Systems considered—(a) La-terminated LLZO (Li: blue spheres, La: yellow, Zr: green, O: red), (b) GaAs (111) (Ga: red, As: green), (c) Al (111), and (d) Na adsorbed on Al (111) (Al: blue, Na: yellow). The locations  $Z_A$  and  $Z_B$  denote the metal–vacuum interfaces for the CPD setup. Furthermore, the external potential bias  $\delta V$  across  $Z_B - Z_A$  is  $\delta V_{\text{app}}$  in the CEF setup and  $\delta \tilde{\phi}$  in the CPD setup.

favorable terminations in a previous study,<sup>72</sup> which consists of 12 formula units of  $\text{Li}_7\text{La}_3\text{Zr}_2\text{O}_{12}$ . LLZO is an insulating system and has applications as a solid electrolyte in lithium-based batteries, and we employ  $\Gamma$ -point sampling for Brillouin zone integration. (b) **GaAs (111) slab**—consists of four alternating layers of Ga and As atoms, comprising 24 atoms. The slab is polar with Ga and As terminations on opposite surfaces. The bulk crystal structure was obtained from the Materials Project database,<sup>73</sup> and is well-known to be a

semiconducting material with applications in electronic devices. For Brillouin zone integration, we used a  $10 \times 10 \times 1$  Monkhorst–Pack grid. (c) **Al (111) slab**—comprising four layers of the FCC structure with a total of 32 Al atoms. We used the bulk geometry of this metallic system from the Materials Project database.<sup>73</sup> We use a  $12 \times 12 \times 1$  Monkhorst–Pack grid for Brillouin zone integration. As a sample system to model a simple adsorption process, we evaluated the adsorption energy of Na on Al (111). Note that we place the adsorbed Na at a distance of 5 bohr “above” the “top” layer of Al atoms in the (111) slab (see panel d in Figure 4). We limit the maximum external electric field to 0.2 V/ $\text{\AA}$  for the LLZO slab and 0.15 V/ $\text{\AA}$  for the GaAs slab, where these limits are determined based on the bulk calculated band gap and the slab thickness to ensure there is no dielectric breakdown.

**3.1. Validation of the CEF Setup.** In this subsection, we benchmark the CEF setup implemented in DFT-FE as described in Section 2.2.1 with that of the constant electric field setup<sup>9,47</sup> used in QE. For various magnitudes of external electric field  $\mathcal{E}$ , we compare the DFT internal energy, ionic forces, and dipole moments between the two codes. The dipole moment ( $\mu$ ) is computed relative to the center of the simulation domain as  $\mu_z = \int_{\Omega_p} (b(\mathbf{x}) + \rho(\mathbf{x})) z d\mathbf{x}$ , where  $z$  represents the position along the nonperiodic axis. We follow the convention that electron density ( $\rho(\mathbf{x})$ ) is positive while the nuclear charge density ( $b(\mathbf{x})$ ) is negative. The internal energy and forces are computed as per eqs 17 and 18, respectively.

As discussed in Section 2.2.1, referring to eq 16, the electrostatic problem for the total charge density in the CEF setup is solved using Neumann boundary conditions on the nonperiodic boundaries, with an additional zero-mean value constraint to fix the electrostatic potential reference.  $\mathcal{E}$  is included in the DFT Hamiltonian using the auxiliary potential,  $V_{\text{app}}$ . In contrast, periodic boundary conditions are used in the QE when computing the electrostatic potential. However, a nonzero dipole moment in the system results in artificial electric fields in QE and is mitigated using a dipole correction scheme<sup>9</sup> in the course of the self-consistent-field iteration. The potential corresponding to the constant external electric field is of sawtooth form in both DFT-FE and QE, with maximum and

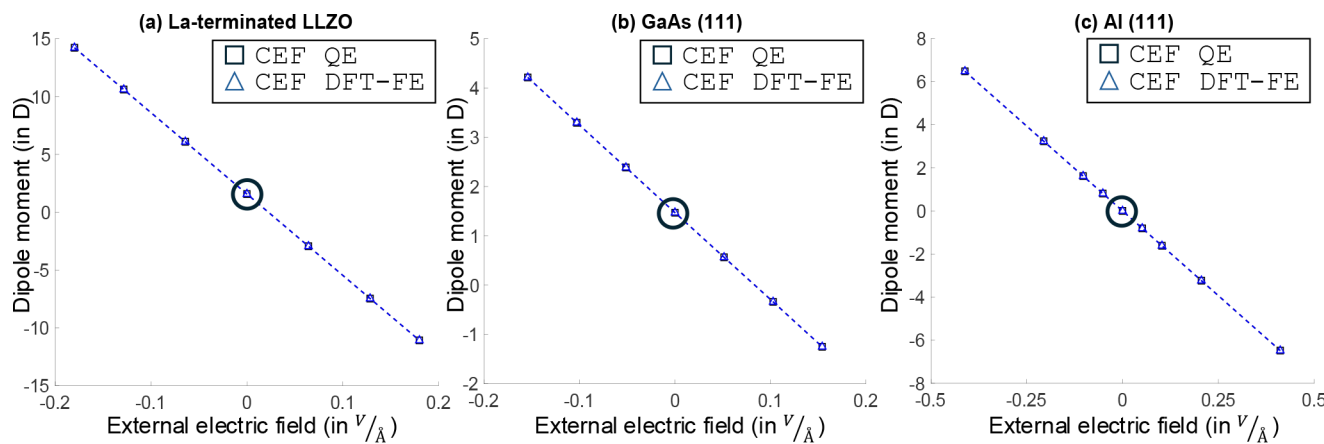


**Figure 5.** Dielectric response comparison of CEF in DFT-FE (triangles) against sawtooth potential with a dipole correction in QE (squares). The plots show the dipole moment ( $\mu$ ) in units of debye ( $D$ ) as a function of applied external field ( $\mathcal{E}$ ) in V/ $\text{\AA}$  for (a) La-terminated LLZO, (b) GaAs (111), and (c) Al (111). The plots also highlight the dipole moment at zero external electric field.

minimum values positioned at 0.1 fractional units from the simulation boundaries.

**Figure 5** compares the dielectric response of CEF implemented in DFT-FE, against the setup in QE for (a) La-terminated LLZO, (b) GaAs (111), and (c) Al (111) slabs. The slope of the dipole moment against the external electric field quantifies the material's polarization ( $\alpha_z = \frac{\Delta\mu}{\Delta\mathcal{E}}$ ). **Table 1**

**Table 1. Comparison of Polarization ( $\alpha_z$ ) and Dipole Moment ( $\mu$ ) at Zero External Electric Field ( $\mathcal{E} = 0.0$ ) for the Benchmark Systems**

system	$\alpha_z$ (in bohr <sup>3</sup> )		$\mu$ at $\mathcal{E} = 0$ (in D)	
	QE	DFT-FE	QE	DFT-FE
La-terminated LLZO	1422.19	1422.27	1.5764	1.5756
GaAs (111)	357.89	357.92	1.4689	1.4713
Al (111)	318.56	318.62	$1.95 \times 10^{-5}$	$1.98 \times 10^{-5}$

compiles the calculated dipole moments ( $\mu$ ) for all systems at zero external electric field ( $\mathcal{E} = 0$ ) with DFT-FE and QE. For the Al (111) slab, the presence of inversion symmetry results in a nearly vanishing dipole moment at  $\mathcal{E} = 0$ . In contrast, for the La-terminated LLZO and GaAs (111) slabs, nonzero dipole moments of 1.57 and 1.47 D, respectively, are observed. These nonzero dipole moments highlight the importance of boundary conditions imposed: the presence of a large nonzero dipole moment suggests that if short circuit boundary conditions (i.e., periodic or homogeneous Dirichlet) were imposed on the total electrostatic potential ( $\tilde{\phi}(\mathbf{x})$ ), as would be the case in the CPD setup, the resulting ground-state obtained would be different. Hence, we emphasize that by imposing zero-Neumann boundary conditions (or open circuit boundary conditions) for slabs, we ensure that the electrostatic potential can adjust naturally, leading to a physically accurate description of the ground state.

Furthermore, from **Tables S2–S4** in **Section S2** of the Supporting Information, we observe a difference of  $O(10^{-6}) \frac{E_h}{\text{atom}}$  in free energy,  $O(10^{-5}) \frac{E_h}{\text{bohr}}$  in ionic forces and  $O(10^{-3})$  D in dipole moment between DFT-FE and QE. The close agreement in ground-state properties leads to excellent consistency in polarizability ( $\alpha_z$ ) between DFT-FE and QE, as shown in **Table 1**, suggesting the equivalency of both approaches in implementing a CEF. Having validated the CEF setup, we next compare this setup with the CPD setup, a more natural way of applying an external potential difference. We considered the same representative benchmark systems for the study.

**3.2. Comparison between CEF and CPD Setups.** In this section, we compare CEF and CPD setups of applying an

external potential bias by analyzing planar average electron density ( $\rho^0(z)$ ) and planar average bare potential ( $V_{\text{bare}}^0(z)$ ), where  $V_{\text{bare}}(\mathbf{x})$  is defined as  $V_{\text{bare}}(\mathbf{x}) = \tilde{\phi}(\mathbf{x}) + V_{\text{app}}(\mathbf{x})$  with  $\tilde{\phi}(\mathbf{x}) = \phi(\mathbf{x}) + (V_{\text{loc}}(\mathbf{x}) - V_{\text{self}}(\mathbf{x}))$  denoting the total electrostatic potential due to electron and nuclear charge density. Specifically,  $\rho^0(z)$  and  $V_{\text{bare}}^0(z)$  are computed as follows,

$$\rho^0(z) = \int_{S_z} \rho(\mathbf{x}) dxdy, \quad V_{\text{bare}}^0(z) = \frac{1}{A_z} \int_{S_z} V_{\text{bare}}(\mathbf{x}) dxdy \quad (21)$$

where  $S_z$  denotes the planar surface within the simulation domain located at position  $z$  along the nonperiodic axis, while  $A_z$  corresponds to the area of  $S_z$ . Note that  $V_{\text{app}}(\mathbf{x})$  denotes the applied potential arising due to the constant electric fields across the slab. As discussed in **Section 2.2.1**, CEF setup introduces  $V_{\text{app}}$  as a sawtooth potential with slope  $-\mathcal{E}$  across the slab. In contrast, the CPD setup (see **Section 2.2.2**) imposes the external potential bias as a constraint on the electrostatic potential ( $\tilde{\phi}$ ) at a distance of  $L_w$  from the slab surface (see **Figure 2**), while  $V_{\text{app}} = 0$  throughout the simulation domain. We position the metal-vacuum interface at  $L_w = 10$  bohr from the slab's surface to provide a sufficiently thick vacuum region that minimizes electron density penetration into the conductor, since the atomic valence density, as obtained from the pseudopotential file,<sup>69,70</sup> remains below  $5 \times 10^{-6} \frac{e}{\text{bohr}^3}$  at  $L_w = 10$  bohr. **Table 2** shows the external potential bias imposed for the various systems considered, and this corresponds to an electric field of  $\mathcal{E} = 0.1 \frac{V}{\text{\AA}}$  for La-terminated LLZO and GaAs (111) and  $\mathcal{E} = 0.15 \frac{V}{\text{\AA}}$  for Al (111) with and without Na adsorbed in the CEF setup.

**Figures 6** and **7** show the plot of the difference in the ground-state planar average electron density ( $\Delta\rho^0(z) = \rho^0_{\text{CEF}}(z) - \rho^0_{\text{CPD}}(z)$ ) and planar average bare potential ( $\Delta V_{\text{bare}}^0(z) = V_{\text{bare}}^0_{\text{CEF}}(z) - V_{\text{bare}}^0_{\text{CPD}}(z)$ ). Additionally, **Table 2** compares the differences in dipole moments ( $\mu$ ), free energies ( $\Delta E$ ), and ionic forces ( $\Delta F$ ) between the two setups studied in this work. For the case of Al (111) slab, with or without Na adsorbed, the intrinsic metallic screening results in negligible difference in  $V_{\text{bare}}$  within the slab region between the two setups (**Figure 6**), while a similarly strong internal screening is also observed in GaAs (111) slab, where no significant variation in  $V_{\text{bare}}$  is observed within the slab between the two setups. In contrast, the insulating La-terminated LLZO slab shows a significant difference in  $V_{\text{bare}}$  between the two setups within the slab region (**Figure 7**).

As discussed earlier in this subsection, the potential bias is applied such that the potential at  $Z_A$  is higher than that of  $Z_B$

**Table 2. Comparison of  $\delta V_{\text{bare}}^0$  Compared to the Target Value, Dipole Moments ( $\mu$ ), Differences in Free Energies ( $\Delta E$ ), and Ionic Forces ( $\Delta F$ ) between the CEF and CPD Setups for the Benchmark Systems Considered**

system	target $\delta V$ (in $\frac{E_h}{e}$ )	$\delta V_{\text{bare}}^0$ (in $\frac{E_h}{e}$ )		$\mu$ (in D)		$\Delta E$ (in $\frac{E_h}{\text{atom}}$ )	$\Delta F$ (in $\frac{E_h}{\text{bohr}}$ )
		CEF	CPD	CEF	CPD		
La-terminated LLZO	-0.143	-0.072	-0.143	8.2	19.39	$3.51 \times 10^{-5}$	$4.04 \times 10^{-3}$
GaAs (111)	-0.072	-0.008	-0.072	3.3	8.64	$2.22 \times 10^{-4}$	$7.78 \times 10^{-4}$
Al (111)	-0.099	-0.040	-0.099	2.43	6.08	$1.42 \times 10^{-4}$	$9.73 \times 10^{-5}$
Al (111) + Na	-0.113	-0.021	-0.113	5.5	13.83	$3.81 \times 10^{-4}$	$2.6 \times 10^{-3}$

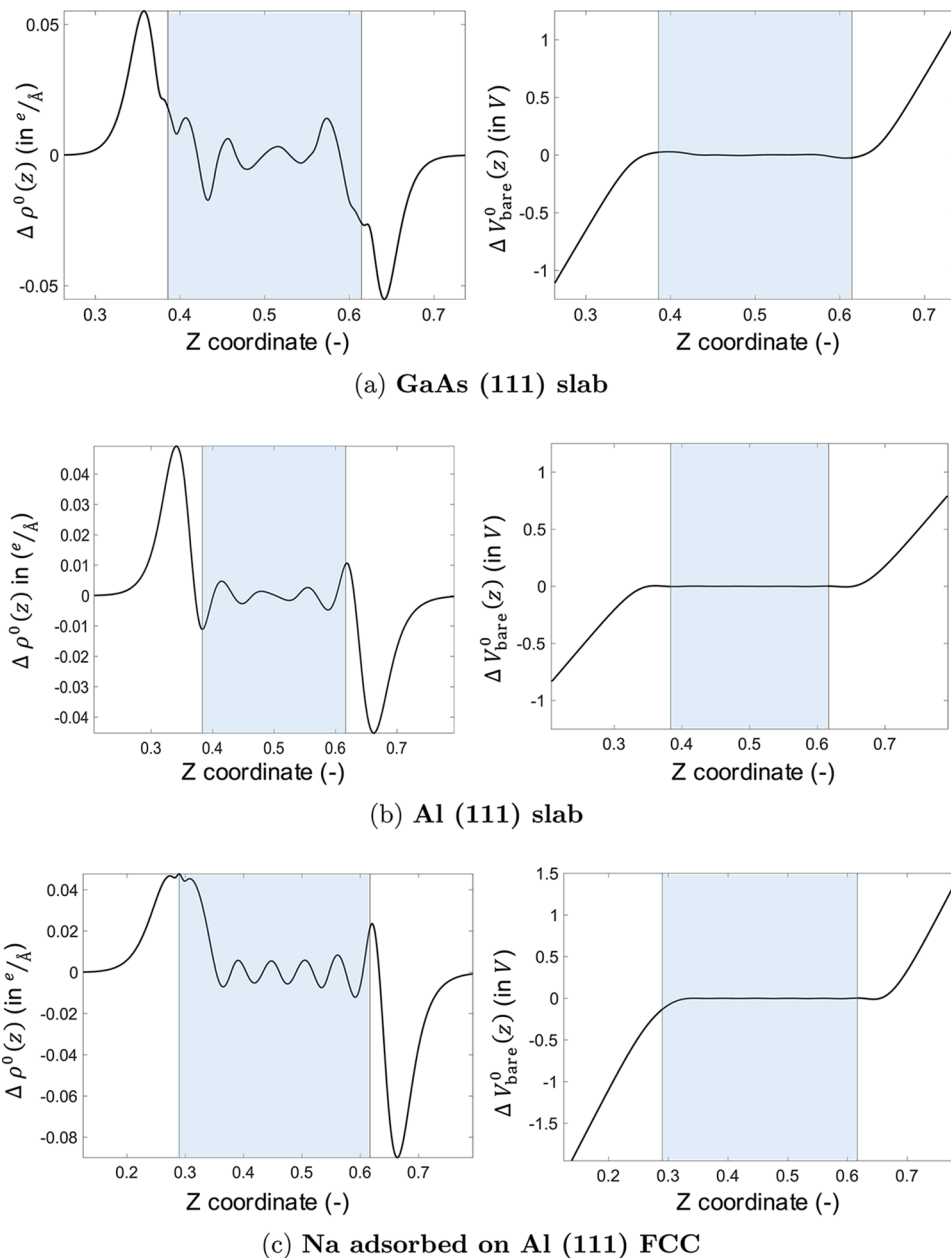


**Figure 6.** Comparison of CEF against CPD. The shaded region depicts the region of the slab. The plot on the left shows  $\Delta\rho^0(z)$  with respect to the  $z$ -coordinate in fractional units, while the plot on the right shows  $\Delta V_{\text{bare}}^0(z)$  with respect to the  $z$ -coordinate in fractional units. We offset  $V_{\text{bare}}^0(z)$  such that  $V_{\text{bare}}^0(0.5) = 0$ , aligning the reference for both potentials.

(see Figures 1 and 2). Consequently, we observe the electron density, and hence the dipole moment ( $\mu$ ), to shift toward  $Z_B$ . Furthermore,  $\mu$  values in Table 2 indicate that the shifts in  $\mu$  for the CPD setup are greater than CEF, which is due to the fact that the CPD setup precisely maintains the target potential bias, while  $\delta V_{\text{bare}}^0$  is lower in the CEF setup. The  $\delta V_{\text{bare}}^0$  being lower than the target value in the CEF setup is expected since  $\delta V_{\text{app}} (\neq \delta V_{\text{bare}}^0)$  is obtained via the electric field  $\mathcal{E}$ , which is the controlling parameter. On the other hand,  $\delta \tilde{\phi} (= \delta V_{\text{bare}}^0)$  is the controlling parameter in the CPD setup. As a consequence, we treat the control parameters, namely  $\mathcal{E}$  or  $\delta V_{\text{app}}$  in CEF and  $\delta V_{\text{bare}}^0$  or  $\delta \tilde{\phi}$  in CPD, for each setup separately, and emphasize that for experimental setups where the total electrostatic potential ( $\tilde{\phi}$ ) across the surface or interface is controlled, the CPD setup is a natural choice in the modeling strategy. In the

next subsection, we present the surface energies and adsorption energies using both setups.

**3.3. Surface and Adsorption Energies: CEF vs CPD.** In this section, we examine the relaxed surface energies of the La-terminated LLZO surface and GaAs (111) surface at various external potential biases. Furthermore, we also investigate the effect of external potential bias on the adsorption energy of Na on the Al (111) surface. We compare the surface energies ( $\gamma$ ) and adsorption energies ( $E_{\text{ads}}$ ) obtained between the two setups, CEF and CPD. All relaxed structures are obtained using the LBFGS algorithm until the atomic forces are below  $4 \times 10^{-4} \frac{E_h}{\text{bohr}}$ , ensuring well-converged structures for subsequent analyses.

**3.3.1. Comparison of Surface Energies.** The surface energy ( $\gamma$ ) in  $\text{J/m}^2$  is computed from DFT as

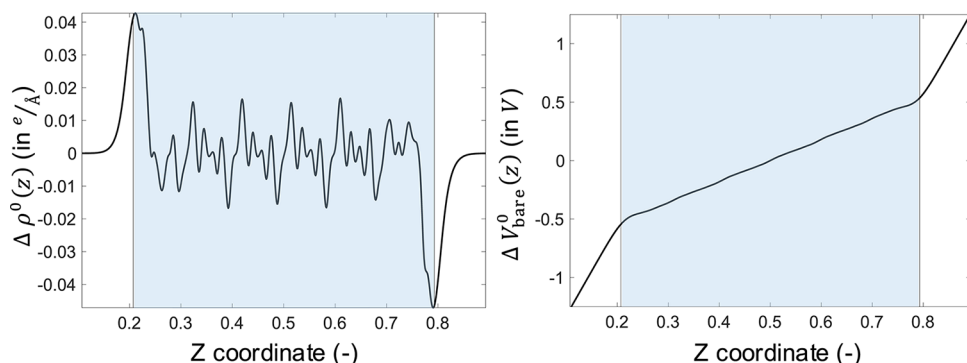


**Figure 7.** La-terminated LLZO slab. Comparison of CEF against CPD. The shaded region depicts the region of the slab. The plot on the left shows  $\Delta\rho^0(z)$  with respect to the  $z$ -coordinate in fractional units, while the plot on the right shows  $\Delta V_{\text{bare}}^0(z)$  with respect to the  $z$ -coordinate in fractional units. We offset  $V_{\text{bare}}^0(z)$  such that  $V_{\text{bare}}^0(0.5) = 0$ , aligning the reference for both potentials.

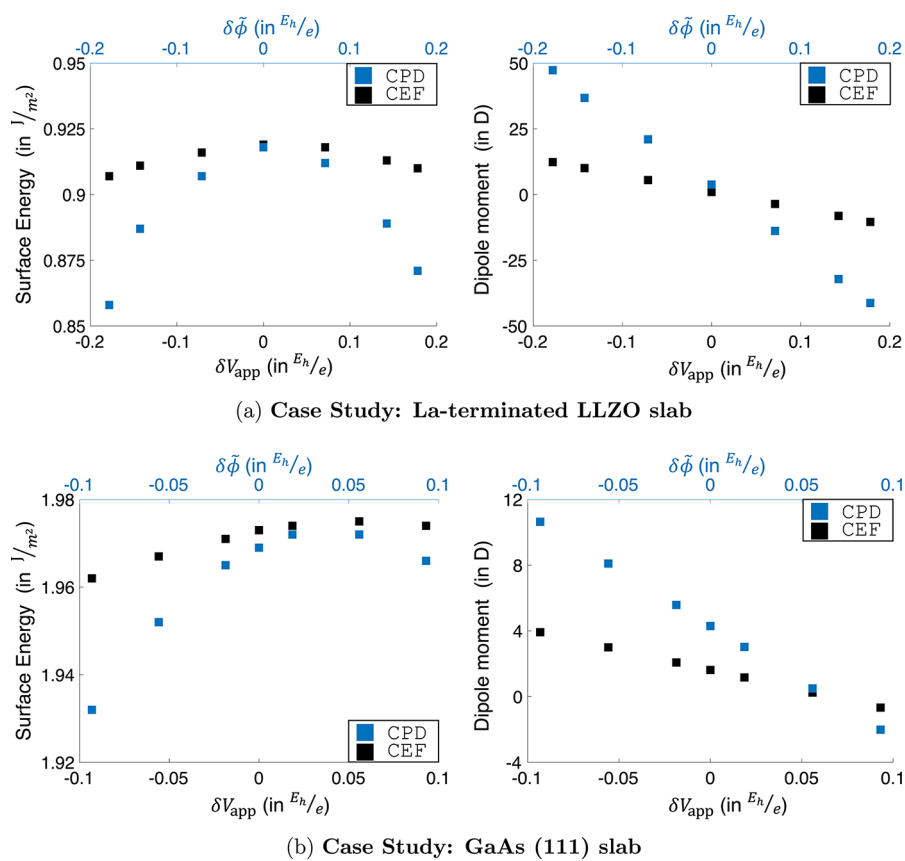
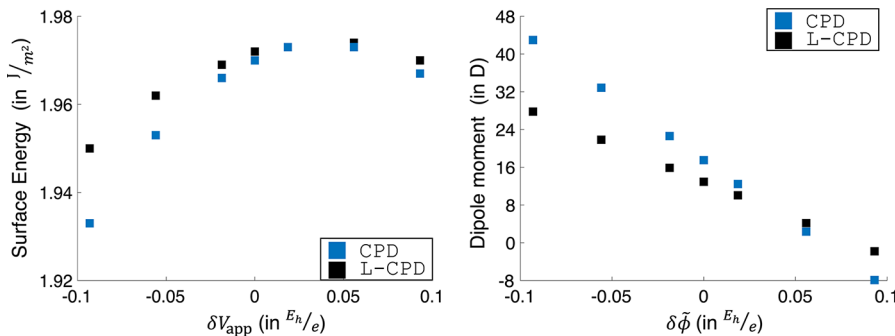


**Figure 8.** Comparison of surface energy (in  $\text{J}/\text{m}^2$ ) and dipole moment (in debye) between CEF and CPD setups. The systems considered are (a) La-terminated LLZO (top row) and (b) GaAs (111) slab (bottom row). The control parameters,  $\delta V_{\text{app}}$  (black) for CEF and  $\delta \tilde{\phi}$  (blue) for CPD are shown as separate  $x$ -axes.

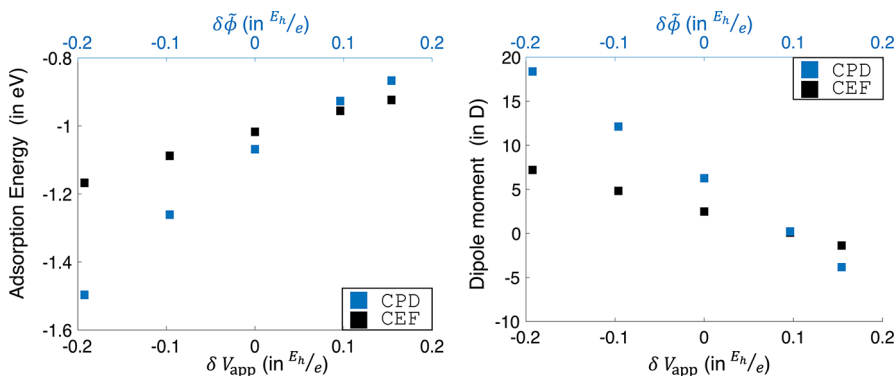
$\gamma(\delta V) = \frac{1}{2A} \left[ E_{\text{slab}}(\delta V) - \frac{N}{N_{\text{bulk}}} E_{\text{bulk}} \right]$ , where  $A$  denotes the surface area in  $\text{m}^2$ .  $E_{\text{slab}}(\delta V)$  and  $E_{\text{bulk}}$  are the DFT total energies of the relaxed slab and bulk structures, with  $\frac{N}{N_{\text{bulk}}}$  indicating the ratio of the number of formula units present in the slab to the number of formula units in the bulk unit cell. In the CEF setup, the potential bias is such that  $\delta V_{\text{app}} = \delta V$ , while for the CPD setup, the total electrostatic potential difference satisfies  $\delta \tilde{\phi} = \delta V$  (see Figures 1 and 2).

Figure 8 compares the surface energies ( $\gamma$ ) and dipole moments ( $\mu$ ) for the La-terminated LLZO and GaAs (111)

slabs. Note that each panel in Figure 8 shows the control parameter  $\delta V_{\text{app}}$  (bottom  $x$ -axis) for CEF and  $\delta \tilde{\phi}$  (top  $x$ -axis) for CPD separately. From Figure 8a for La-terminated LLZO, we observe that the surface energy of CPD is consistently lower than CEF. Moreover, the difference in surface energies increases with increasing magnitude of potential difference, with a maximum difference of  $0.049 \text{ J}/\text{m}^2$  at a potential difference ( $\delta V_{\text{app}}$ ) of  $-0.178 E_h/e$ . A similar trend is observed in Figure 8b for the GaAs (111) slab, where the surface energy computed in the CPD setup is consistently lower than CEF, with the maximum difference in  $\gamma$  of  $0.03 \text{ J}/\text{m}^2$ . The minimum difference in  $\gamma$  between the two setups occurs at a positive bias



**Figure 9.** Comparison of surface energy (in  $\text{J/m}^2$ ) and dipole moment (in debye) between CPD and L-CPD setups in a  $2 \times 2 \times 1$  GaAs (111) slab. Since a  $2 \times 2 \times 1$  supercell is considered, the dipole moment is  $4\times$  that in Figure 8.



**Figure 10.** Comparison of adsorption energy (in eV) and dipole moment (in debye) between CEF and CPD. The adsorption energy of Na on the Al (111) surface is computed along with the dipole moment of the relaxed Al (111) slab at various external potential biases. The control parameters  $\delta V_{\text{app}}$  (black) for CEF and  $\delta \tilde{\phi}$  (blue) for CPD are shown as separate x-axes.

of  $0.018 E_h/e$  for GaAs (111), while the minimum difference in  $\gamma$  for LLZO occurs at zero bias. Additionally, for both the LLZO and GaAs, we observe the variation of dipole moment ( $\mu$ ) of relaxed structures in the CPD setup to exhibit a steeper variation with applied bias than the CEF. The steeper variation of  $\mu$  in CPD is in line with our previous observation of a larger dipole shift in the CPD setup, as described in Section 3.2. The differences observed in  $\gamma$  and  $\mu$  between the two setups indicate fundamental differences in interpreting an applied potential bias across a system and the importance of the different control parameters involved.

To demonstrate the differences in surface energies obtained with the L-CPD setup against the CPD setup, we compare the surface energies of the  $2 \times 2 \times 1$  supercell of the GaAs slab as a function of the applied potential ( $\delta \tilde{\phi}$ ), as shown in Figure 9. Importantly, we observe that the CPD setup always has lower surface energy, and the variation of dipole moment is steeper in the CPD setup than in the L-CPD setup. These trends are consistent with the fact that the potential is applied over a larger surface area in the CPD setup compared to the L-CPD approach, which allows for a larger modification of the underlying electronic structure in CPD versus L-CPD, resulting in a lowering of the surface energy and a larger change in the dipole moment. Additionally, we observe that the trends in surface energy and dipole moment corresponding to the L-CPD setup lie between the CEF and CPD setups.

**3.3.1.1. Adsorption Energy.** The adsorption energy ( $E_{\text{ads}}$ ) of Na on Al (111) surface is computed as  $E_{\text{ads}}(\delta V) = [E_{\text{slab}}^{\text{Al+Na}}(\delta V) - E_{\text{slab}}^{\text{Al}}(\delta V) - E_{\text{Na}}^{\text{vacuum}}]$ , where  $E_{\text{slab}}^{\text{Al+Na}}(\delta V)$  denotes the DFT internal energy of Na atom on Al (111) slab and  $E_{\text{slab}}^{\text{Al}}(\delta V)$

denotes the internal energy of Al (111) slab at external potential bias  $\delta V$ .  $E_{\text{Na}}^{\text{vacuum}}$  is the internal energy of a single Na atom in a vacuum without any potential bias. We ensure that the locations ( $Z_A$  and  $Z_B$ ) of the metal-vacuum interface for both Na on the Al (111) slab and the standalone Al (111) slab are the same, with  $\Delta Z = Z_A - Z_B = 33.8$  bohr.

Figure 10 compares the adsorption energy ( $E_{\text{ads}}$ ) and dipole moments ( $\mu$ ) of the relaxed structures of Na adsorbed on Al (111) and Al (111) slabs for both setups. Similar to the surface energy plots (Figure 8), the panels in Figure 10 show the control parameter  $\delta V_{\text{app}}$  (bottom x-axis) for CEF and the control parameter  $\delta \tilde{\phi}$  (top x-axis) for CPD separately. From Figure 10, we observe that the adsorption is favourable at negative potential biases in both setups, which can be attributed to Na being near the  $Z_A$  interface and adsorbs on the Al by partial electron transfer (see Figure 4) to the Al slab. Under a positive bias, the electron density is drawn toward the Na atom, inhibiting further transfer of electrons and thereby weakening the ability of Na to get adsorbed. In contrast, a negative bias redistributes electron density away from the Na site, promoting charge transfer and strengthening Na adsorption. Additionally, from Figure 10, we observe that the change in Na adsorption energy is more sensitive to the applied bias in the CPD setup than in the CEF setup. Similarly, we observe a steeper variation in the  $\mu$  of relaxed structures versus applied bias in the CPD setup compared to that in CEF, in agreement with our observation in Section 3.2.

#### 4. PERSPECTIVES AND CONCLUDING REMARKS

Accurate and efficient first-principles modeling of surfaces and interfaces is essential for gaining theoretical insights into essential processes such as charge transfer, reaction kinetics, material stability, and polarization, which are highly important to understand and optimize in applications such as catalysis, batteries, fuel cells, sensors, and electronics. While PW-DFT has long been the preferred method for first-principles simulations, the inherent restriction in plane-wave methodologies to impose periodic boundary conditions leads to undesirable consequences such as spurious image–image interactions and the emergence of artificial electric fields in the case of systems with a net dipole. Moreover, plane-wave-based codes exhibit poor scalability on multinode CPU-GPU architectures, restricting the system sizes that can be handled. In contrast, real-space FE methods employed in this work can accommodate generic boundary conditions and have demonstrated an exceptional ability to scale on massively parallel supercomputing architectures across the world. The ability of DFT-FE to efficiently handle large systems and accommodate generic boundary conditions presents new opportunities for modeling surfaces and interfaces with minimal approximations, which has been leveraged in this work for modeling surfaces and interfaces.

The control of external parameters, such as potential bias, solvation effects, and their combination, plays a critical role in tailoring the properties of slabs and interfaces. PW-DFT calculations using a constant electric field<sup>44,45,47</sup> have provided insights on controlling properties such as surface diffusion, polarization, and ferroelectricity. Additionally, the effective screening medium (ESM) method<sup>50</sup> in PW-DFT decouples the periodicity of the electrostatic potential by analytically solving for the electrostatic potential using the Green's function approach with nonperiodic boundary conditions. This method provides flexibility in modeling surfaces and interfaces by introducing a generic framework to control potential bias, solvation effects, or their combination. However, when employed in conjunction with PW-DFT, the ESM method is suited for those problems with boundary conditions whose Green's function are readily available and further assumes that the mean field effective potential is short-ranged, which is not necessarily true when exact exchange<sup>74</sup> or van der Waals<sup>75</sup> functionals are employed. Consequently, employing semiperiodic boundary conditions is essential for the accurate modeling of surfaces and interfaces without any spurious periodic interactions in the presence of a potential bias.

Addressing the above limitations and to model larger-scale systems involving surfaces and interfaces, we implement in DFT-FE two setups of applying an external potential bias: (i) constant electric field (CEF) and (ii) constrained potential difference (CPD). These setups, in contrast to the NEGF (nonequilibrium Green's function)<sup>76</sup> formulation, ensure that the electrons are in the ground state and the electronic current is negligible. We benchmark and validate the CEF setup with the constant electric field setup in QE by comparing ground-state properties such as internal energy, ion forces, and dipole moment. We observe an excellent agreement in the ground-state properties for the benchmark systems considered, namely, LLZO, GaAs, and Al.

In the CEF setup, a constant electric field ( $\mathcal{E}$ ) is applied along the nonperiodic direction in DFT-FE. The DFT Hamiltonian is modified by introducing an auxiliary linear

potential,  $V_{\text{app}}(\mathbf{x})$ , such that the slope of this linear potential equals  $-\mathcal{E}$ . Furthermore, the electrostatic potential arising from the electron and nuclear densities is obtained by solving Poisson's problem with zero-Neumann boundary conditions on boundaries parallel to the slab surface. Additionally, a zero mean-value constraint is imposed to fix the reference of the electrostatic potential ( $\phi(\mathbf{x})$ ). In this setup, the modeling of surfaces and interfaces in vacuum can be accomplished by setting the external electric field to zero ( $\mathcal{E} = 0$ ).

In contrast to the CEF setup, the CPD setup directly enforces the desired (experimental) potential bias by imposing constraints on the total electrostatic potential ( $\tilde{\phi}(\mathbf{x})$ ). Note that the CPD setup can be modified to include solvation effects<sup>77,78</sup> with appropriate changes to the Poisson problem to determine the total electrostatic potential. The two setups (CEF and CPD) control different parameters ( $\delta V_{\text{app}}$  and  $\delta \tilde{\phi}$ , respectively) and hence have different electronic ground-states as demonstrated in Figures 6 and 7. Additionally, the L-CPD setup, an extension of the CPD setup, is proposed by localizing the region where  $\delta \tilde{\phi}$  is controlled, which can have implications in modeling physical systems exposed to potential differences in localized regions. Note that the L-CPD setup demonstrated in this work cannot be trivially implemented in PW-DFT.

To further contrast the two setups (CEF and CPD), we compared the planar average electron density ( $\rho^0(z)$ ) and bare potential of our representative systems. We observed for (111) Al FCC and (111) GaAs a similar behavior of  $V_{\text{bare}}^0(z)$  within the slab due to screening effects, while for the La-terminated LLZO slab, we noticed a significant difference in  $V_{\text{bare}}^0(z)$  in the region of the slab. For all of the systems considered, we observed that the dipole moment response to the potential bias was stronger in the CPD setup than in CEF, resulting in steeper variations in surface and adsorption energies with applied bias. Overall, the CPD setup consistently demonstrates greater sensitivity to the external potential bias in both surface energy and adsorption energy calculations compared to the CEF setup and should represent experimental scenarios of an applied potential bias better. Finally, the two setups (CEF and CPD) as implemented in DFT-FE offer a robust framework for investigating surfaces and interfaces without any underlying assumptions or correction schemes, while also enabling simulations that scale better with available computational resources compared to most state-of-the-art PW-DFT codes.

#### ■ ASSOCIATED CONTENT

##### Data Availability Statement

All input and output calculation files that yielded the results presented in this work are available freely online in our GitHub repository ([https://github.com/matrixlabiisc/](https://github.com/matrixlabiisc/AppliedPotentialBias_JCTC) AppliedPotentialBias\_JCTC).

##### SI Supporting Information

The Supporting Information is available free of charge at <https://pubs.acs.org/doi/10.1021/acs.jctc.5c00513>.

List of pseudopotentials used and comparison of differences in free energies, ionic forces, and dipole moments between QE and DFT-FE in the three systems considered (PDF)

## AUTHOR INFORMATION

### Corresponding Authors

**Gopalakrishnan Sai Gautam** — Department of Materials Engineering, Indian Institute of Science, Bengaluru 560012, India;  [orcid.org/0000-0002-1303-0976](https://orcid.org/0000-0002-1303-0976); Email: [saigautamg@iisc.ac.in](mailto:saigautamg@iisc.ac.in)

**Phani Motamarri** — Department of Computational and Data Sciences, Indian Institute of Science, Bengaluru 560012, India;  [orcid.org/0000-0003-3160-7334](https://orcid.org/0000-0003-3160-7334); Email: [phanim@iisc.ac.in](mailto:phanim@iisc.ac.in)

### Author

**Kartick Ramakrishnan** — Department of Computational and Data Sciences, Indian Institute of Science, Bengaluru 560012, India;  [orcid.org/0000-0003-3155-157X](https://orcid.org/0000-0003-3155-157X)

Complete contact information is available at:

<https://pubs.acs.org/10.1021/acs.jctc.5c00513>

### Notes

The authors declare no competing financial interest.

## ACKNOWLEDGMENTS

P.M. gratefully acknowledges the seed grant from the Indian Institute of Science and the SERB Startup Research Grant from the Department of Science and Technology, India (Grant Number: SRG/2020/002194), which supported the purchase of GPU clusters used in the current work. P.M. and G.S.G. acknowledge National Supercomputing Mission (NSM) R&D for the exascale grant (DST/NSM/R&D Exascale/2021/14.02) that supported the use of PARAM Pravega supercomputer at the Indian Institute of Science. This research also used computational resources at the Argonne and the Oak Ridge Leadership Computing Facilities. The Argonne Leadership Computing Facility at Argonne National Laboratory is supported by the Office of Science of the U.S. DOE under Contract No. DE-AC02-06CH11357. The Oak Ridge Leadership Computing Facility at the Oak Ridge National Laboratory is supported by the Office of Science of the U.S. DOE under Contract No. DE-AC05-00OR22725. A portion of the calculations in this work used computational resources of the supercomputer Fugaku provided by RIKEN through the HPCI System Research Project. K.R. acknowledges the Prime Minister Research Fellowship (PMRF) from the Ministry of Education, India, for financial support. P.M. acknowledges the Google India Research Award 2023 for financial support during the course of this work.

## REFERENCES

- (1) Hammer, B.; Nørskov, J. *Impact of Surface Science on Catalysis; Advances in Catalysis*; Academic Press, 2000; 45; 71–129.
- (2) Zhang, Z.; Yates, J. T. J. Band Bending in Semiconductors: Chemical and Physical Consequences at Surfaces and Interfaces. *Chem. Rev.* **2012**, *112*, 5520–5551.
- (3) Peled, E.; Menkin, S. Review—SEI: Past, Present and Future. *J. Electrochem. Soc.* **2017**, *164*, A1703.
- (4) Xiao, Y.; Wang, Y.; Bo, S.-H.; Miara, L. J.; Ceder, G. Understanding interface stability in solid-state batteries. *Nat. Rev. Mater.* **2020**, *5*, 105–126.
- (5) Oguzie, E. E.; Li, Y.; Wang, S. G.; Wang, F. Understanding corrosion inhibition mechanisms-experimental and theoretical approach. *RSC Adv.* **2011**, *1*, 866–873.
- (6) Kresse, G.; Furthmüller, J. Efficient iterative schemes for ab initio total-energy calculations using a plane-wave basis set. *Phys. Rev. B* **1996**, *54*, 11169–11186.
- (7) Kaplan, A. D.; Levy, M.; Perdew, J. P. The Predictive Power of Exact Constraints and Appropriate Norms in Density Functional Theory. *Annu. Rev. Phys. Chem.* **2023**, *74*, 193–218.
- (8) Freysoldt, C.; Mishra, A.; Ashton, M.; Neugebauer, J. Generalized dipole correction for charged surfaces in the repeated-slab approach. *Phys. Rev. B* **2020**, *102*, No. 045403.
- (9) Bengtsson, L. Dipole correction for surface supercell calculations. *Phys. Rev. B* **1999**, *59*, 12301–12304.
- (10) Neugebauer, J.; Scheffler, M. Adsorbate-substrate and adsorbate-adsorbate interactions of Na and K adlayers on Al(111). *Phys. Rev. B* **1992**, *46*, 16067–16080.
- (11) Rozzi, C. A.; Varsano, D.; Marini, A.; Gross, E. K. U.; Rubio, A. Exact Coulomb cutoff technique for supercell calculations. *Phys. Rev. B* **2006**, *73*, No. 205119.
- (12) Vijay, S.; Schlipf, M.; Miranda, H.; Karsai, F.; Kaltak, M.; Marsman, M.; Kresse, G. Efficient periodic density functional theory calculations of charged molecules and surfaces using Coulomb kernel truncation. *arXiv* **2023**.
- (13) Kronik, L.; Makmal, A.; Tiago, M. L.; Alemany, M. M. G.; Jain, M.; Huang, X.; Saad, Y.; Chelikowsky, J. R. PARSEC — the pseudopotential algorithm for real-space electronic structure calculations: recent advances and novel applications to nano-structures. *Phys. Status Solidi B* **2006**, *243*, 1063–1079.
- (14) Michaud-Riou, V.; Zhang, L.; Guo, H. RESCU: A real space electronic structure method. *J. Comput. Phys.* **2016**, *307*, 593–613.
- (15) Ghosh, S.; Suryanarayana, P. SPARC: Accurate and efficient finite-difference formulation and parallel implementation of density functional theory: Isolated clusters. *Comput. Phys. Commun.* **2017**, *212*, 189–204.
- (16) Andrade, X.; Strubbe, D.; De Giovannini, U.; Larsen, A. H.; Oliveira, M. J. T.; Alberdi-Rodriguez, J.; Varas, A.; Theophilou, I.; Helbig, N.; Verstraete, M. J.; Stella, L.; Nogueira, F.; Aspuru-Guzik, A.; Castro, A.; Marques, M. A. L.; Rubio, A. Real-space grids and the Octopus code as tools for the development of new simulation approaches for electronic systems. *Phys. Chem. Chem. Phys.* **2015**, *17*, 31371–31396.
- (17) Enkovaara, J.; Rostgaard, C.; Mortensen, J. J.; Chen, J.; Dulak, M.; Ferrighi, L.; Gavnholt, J.; Glinsvad, C.; Haikola, V.; Hansen, H. A.; Kristoffersen, H. H.; Kuisma, M.; Larsen, A. H.; Lehtovaara, L.; Ljungberg, M.; Lopez-Acevedo, O.; Moses, P. G.; Ojanen, J.; Olsen, T.; Petzold, V.; Romero, N. A.; Stausholm-Møller, J.; Strange, M.; Tritsaris, G. A.; Vanin, M.; Walter, M.; Hammer, B.; Häkkinen, H.; Madsen, G. K. H.; Nieminen, R. M.; Nørskov, J. K.; Puska, M.; Rantala, T. T.; Schiøtz, J.; Thygesen, K. S.; Jacobsen, K. W. Electronic structure calculations with GPAW: a real-space implementation of the projector augmented-wave method. *J. Phys.: Condens. Matter* **2010**, *22*, No. 253202.
- (18) Genovese, L.; Neelov, A.; Goedecker, S.; Deutsch, T.; Ghasemi, S. A.; Willand, A.; Caliste, D.; Zilberman, O.; Rayson, M.; Bergman, A.; Schneider, R. Daubechies wavelets as a basis set for density functional pseudopotential calculations. *J. Chem. Phys.* **2008**, *129*, No. 014109.
- (19) Genovese, L.; Ospici, M.; Deutsch, T.; Méhaut, J. F.; Neelov, A.; Goedecker, S. Density functional theory calculation on many-cores hybrid central processing unit-graphic processing unit architectures. *J. Chem. Phys.* **2009**, *131*, No. 034103.
- (20) Mohr, S.; Ratcliff, L. E.; Boulanger, P.; Genovese, L.; Caliste, D.; Deutsch, T.; Goedecker, S. Daubechies wavelets for linear scaling density functional theory. *J. Chem. Phys.* **2014**, *140*, 204110.
- (21) White, S. R.; Wilkins, J. W.; Teter, M. P. Finite-element method for electronic structure. *Phys. Rev. B* **1989**, *39*, 5819–5833.
- (22) Tsuchida, E.; Tsukada, M. Electronic-structure calculations based on the finite-element method. *Phys. Rev. B* **1995**, *52*, 5573–5578.
- (23) Tsuchida, E.; Tsukada, M. Adaptive finite-element method for electronic-structure calculations. *Phys. Rev. B* **1996**, *54*, 7602–7605.
- (24) Pask, J. E.; Klein, B. M.; Fong, C. Y.; Sterne, P. A. Real-space local polynomial basis for solid-state electronic-structure calculations: A finite-element approach. *Phys. Rev. B* **1999**, *59*, 12352–12358.

- (25) Goedecker, S. Linear scaling electronic structure methods. *Rev. Mod. Phys.* **1999**, *71*, 1085–1123.
- (26) Pask, J. E.; Sterne, P. A. Finite element methods in ab initio electronic structure calculations. *Modell. Simul. Mater. Sci. Eng.* **2005**, *13*, R71.
- (27) Bylaska, E. J.; Holst, M.; Weare, J. H. Adaptive Finite Element Method for Solving the Exact Kohn-Sham Equation of Density Functional Theory. *J. Chem. Theory Comput.* **2009**, *5*, 937–948.
- (28) Suryanarayana, P.; Gavini, V.; Blesgen, T.; Bhattacharya, K.; Ortiz, M. Non-periodic finite-element formulation of Kohn-Sham density functional theory. *J. Mech. Phys. Solids* **2010**, *58*, 256–280.
- (29) Motamarri, P.; Nowak, M.; Leiter, K.; Knap, J.; Gavini, V. Higher-order adaptive finite-element methods for Kohn-Sham density functional theory. *J. Comput. Phys.* **2013**, *253*, 308–343.
- (30) Schauer, V.; Linder, C. All-electron Kohn-Sham density functional theory on hierachic finite element spaces. *J. Comput. Phys.* **2013**, *250*, 644–664.
- (31) Chen, H.; Dai, X.; Gong, X.; He, L.; Zhou, A. Adaptive Finite Element Approximations for Kohn-Sham Models. *Multiscale Model. Simul.* **2014**, *12*, 1828–1869.
- (32) Davydov, D.; Young, T. D.; Steinmann, P. On the adaptive finite element analysis of the Kohn-Sham equations: methods, algorithms, and implementation. *Int. J. Numer. Methods Eng.* **2016**, *106*, 863–888.
- (33) Kanungo, B.; Gavini, V. Large-scale all-electron density functional theory calculations using an enriched finite-element basis. *Phys. Rev. B* **2017**, *95*, No. 035112.
- (34) Kanungo, B.; Gavini, V. Real time time-dependent density functional theory using higher order finite-element methods. *Phys. Rev. B* **2019**, *100*, No. 115148.
- (35) Motamarri, P.; Das, S.; Rudraraju, S.; Ghosh, K.; Davydov, D.; Gavini, V. DFT-FE—A massively parallel adaptive finite-element code for large-scale density functional theory calculations. *Comput. Phys. Commun.* **2020**, *246*, 106853.
- (36) Das, S.; Motamarri, P.; Gavini, V.; Turcksin, B.; Li, Y. W.; Leback, B. Fast, Scalable and Accurate Finite-Element Based Ab Initio Calculations Using Mixed Precision Computing: 46 PFLOPS Simulation of a Metallic Dislocation System. *Proceedings of the International Conference for High Performance Computing, Networking, Storage and Analysis; Association for Computing Machinery*: New York, NY, USA, 2019; 1–11.
- (37) Matveyev, Y.; Mikheev, V.; Negrov, D.; Zarubin, S.; Kumar, A.; Grimley, E. D.; LeBeau, J. M.; Gloskovskii, A.; Tsymbal, E. Y.; Zenkevich, A. Polarization-dependent electric potential distribution across nanoscale ferroelectric Hf<sub>0.5</sub>Zr<sub>0.5</sub>O<sub>2</sub> in functional memory capacitors. *Nanoscale* **2019**, *11*, 19814–19822.
- (38) Yazyev, O. V.; Moore, J. E.; Louie, S. G. Spin Polarization and Transport of Surface States in the Topological Insulators Bi<sub>2</sub>Se<sub>3</sub> and Bi<sub>2</sub>Te<sub>3</sub> from First Principles. *Phys. Rev. Lett.* **2010**, *105*, No. 266806.
- (39) Pan, Y.; Wang, X.; Zhang, W.; Tang, L.; Mu, Z.; Liu, C.; Tian, B.; Fei, M.; Sun, Y.; Su, H.; Gao, L.; Wang, P.; Duan, X.; Ma, J.; Ding, M. Boosting the performance of single-atom catalysts via external electric field polarization. *Nat. Commun.* **2022**, *13*, 3063.
- (40) Che, F.; Gray, J. T.; Ha, S.; Kruse, N.; Scott, S. L.; McEwen, J.-S. Elucidating the Roles of Electric Fields in Catalysis: A Perspective. *ACS Catal.* **2018**, *8*, 5153–5174.
- (41) Famprakis, T.; Canepa, P.; Dawson, J. A.; Islam, M. S.; Masquelier, C. Fundamentals of inorganic solid-state electrolytes for batteries. *Nat. Mater.* **2019**, *18*, 1278–1291.
- (42) Wang, J.; Panchal, A. A.; Sai Gautam, G.; Canepa, P. The resistive nature of decomposing interfaces of solid electrolytes with alkali metal electrodes. *J. Mater. Chem. A* **2022**, *10*, 19732–19742.
- (43) Chang, B.-Y.; Park, S.-M. Electrochemical Impedance Spectroscopy. *Annual Review of Analytical Chemistry* **2010**, *3*, 207–229.
- (44) Feibelman, P. J. Surface-diffusion mechanism versus electric field: Pt/Pt(001). *Phys. Rev. B* **2001**, *64*, No. 125403.
- (45) Meyer, B.; Vanderbilt, D. Ab initio study of BaTiO<sub>3</sub> and PbTiO<sub>3</sub> surfaces in external electric fields. *Phys. Rev. B* **2001**, *63*, No. 205426.
- (46) Galvez-Aranda, D. E.; Seminario, J. M. Ab Initio Study of the Interface of the Solid-State Electrolyte Li<sub>9</sub>N<sub>2</sub>Cl<sub>3</sub> with a Li-Metal Electrode. *J. Electrochem. Soc.* **2019**, *166*, A2048.
- (47) Kunc, K.; Resta, R. External fields in the self-consistent theory of electronic states: a new method for direct evaluation of macroscopic and microscopic dielectric response. *Phys. Rev. Lett.* **1983**, *51*, 686.
- (48) Taylor, C. D.; Wasileski, S. A.; Filhol, J.-S.; Neurock, M. First principles reaction modeling of the electrochemical interface: Consideration and calculation of a tunable surface potential from atomic and electronic structure. *Phys. Rev. B* **2006**, *73*, No. 165402.
- (49) Fu, C. L.; Ho, K. M. External-charge-induced surface reconstruction on Ag(110). *Phys. Rev. Lett.* **1989**, *63*, 1617–1620.
- (50) Otani, M.; Sugino, O. First-principles calculations of charged surfaces and interfaces: A plane-wave nonrepeated slab approach. *Phys. Rev. B* **2006**, *73*, No. 115407.
- (51) Sundaraman, R.; Goddard, I.; William, A.; Arias, T. A. Grand canonical electronic density-functional theory: Algorithms and applications to electrochemistry. *J. Chem. Phys.* **2017**, *146*, 114104.
- (52) Panigrahi, G.; Kodali, N.; Panda, D.; Motamarri, P. Fast hardware-aware matrix-free algorithms for higher-order finite-element discretized matrix multivector products on distributed systems. *Journal of Parallel and Distributed Computing* **2024**, *192*, No. 104925.
- (53) Das, S.; Kanungo, B.; Subramanian, V.; Panigrahi, G.; Motamarri, P.; Rogers, D.; Zimmerman, P.; Gavini, V. Large-Scale Materials Modeling at Quantum Accuracy: Ab Initio Simulations of Quasicrystals and Interacting Extended Defects in Metallic Alloys. *Proceedings of the International Conference for High Performance Computing, Networking, Storage and Analysis; Association for Computing Machinery*: New York, NY, USA, 2023.
- (54) Das, S.; Motamarri, P.; Subramanian, V.; Rogers, D. M.; Gavini, V. DFT-FE 1.0: A massively parallel hybrid CPU-GPU density functional theory code using finite-element discretization. *Comput. Phys. Commun.* **2022**, *280*, No. 108473.
- (55) Ghosh, K.; Ma, H.; Onizhuk, M.; Gavini, V.; Galli, G. Spin–spin interactions in defects in solids from mixed all-electron and pseudopotential first-principles calculations. *npj Comput. Mater.* **2021**, *7*, 123.
- (56) Ramakrishnan, K.; Das, S.; Motamarri, P. Fast and scalable finite-element based approach for density functional theory calculations using projector augmented wave method. *Phys. Rev. B* **2025**, *111*, No. 035101.
- (57) Parr, R. G.; Gadre, S. R.; Bartolotti, L. J. Local density functional theory of atoms and molecules. *Proc. Natl. Acad. Sci. U. S. A.* **1979**, *76*, 2522–2526.
- (58) Martin, R. M. *Electronic structure: basic theory and practical methods*; Cambridge university press, 2020.
- (59) Langreth, D. C.; Mehl, M. J. Beyond the local-density approximation in calculations of ground-state electronic properties. *Phys. Rev. B* **1983**, *28*, 1809–1834.
- (60) Perdew, J. P.; Burke, K.; Ernzerhof, M. Generalized Gradient Approximation Made Simple. *Phys. Rev. Lett.* **1996**, *77*, 3865–3868.
- (61) Hamann, D. R. Optimized norm-conserving Vanderbilt pseudopotentials. *Phys. Rev. B* **2013**, *88*, No. 085117.
- (62) Ashcroft, N. W.; Mermin, N. D. *Solid state physics*; Cengage Learning, 2022.
- (63) Motamarri, P.; Gavini, V. Configurational forces in electronic structure calculations using Kohn-Sham density functional theory. *Phys. Rev. B* **2018**, *97*, No. 165132.
- (64) Giannozzi, P.; Baroni, S.; Bonini, N.; Calandra, M.; Car, R.; Cavazzoni, C.; Ceresoli, D.; Chiarotti, G. L.; Cococcioni, M.; Dabo, I.; Corso, A. D.; de Gironcoli, S.; Fabris, S.; Fratesi, G.; Gebauer, R.; Gerstmann, U.; Gouguassis, C.; Kokalj, A.; Lazzeri, M.; Martin-Samos, L.; Marzari, N.; Mauri, F.; Mazzarello, R.; Paolini, S.; Pasquarello, A.; Paulatto, L.; Sbraccia, C.; Scandolo, S.; Sclauzero, G.; Seitsonen, A. P.; Smogunov, A.; Umari, P.; Wentzcovitch, R. M. QUANTUM ESPRESSO: a modular and open-source software project for quantum simulations of materials. *J. Phys.: Condens. Matter* **2009**, *21*, No. 395502.

- (65) Hughes, T. J. *The finite element method: linear static and dynamic finite element analysis*; Courier Corporation, 2012.
- (66) Bathe, K. J. *Finite Element Procedures*; Prentice Hall International eds.; Prentice Hall International: Englewood Cliffs, 1986.
- (67) Das, S.; Gavini, V. Accelerating self-consistent field iterations in Kohn-Sham density functional theory using a low rank approximation of the dielectric matrix. *Phys. Rev. B* **2023**, *107*, No. 125133.
- (68) Lehtola, S.; Steigemann, C.; Oliveira, M. J.; Marques, M. A. Recent developments in libxc — A comprehensive library of functionals for density functional theory. *SoftwareX* **2018**, *7*, 1–5.
- (69) van Setten, M.; Giantomassi, M.; Bousquet, E.; Verstraete, M.; Hamann, D.; Gonze, X.; Rignanese, G.-M. The PseudoDojo: Training and grading a 85 element optimized norm-conserving pseudopotential table. *Comput. Phys. Commun.* **2018**, *226*, 39–54.
- (70) Shojaei, M. F.; Pask, J. E.; Medford, A. J.; Suryanarayana, P. Soft and transferable pseudopotentials from multi-objective optimization. *Comput. Phys. Commun.* **2023**, *283*, No. 108594.
- (71) Monkhorst, H. J.; Pack, J. D. Special points for Brillouin-zone integrations. *Phys. Rev. B* **1976**, *13*, 5188–5192.
- (72) Canepa, P.; Dawson, J. A.; Sai Gautam, G.; Statham, J. M.; Parker, S. C.; Islam, M. S. Particle Morphology and Lithium Segregation to Surfaces of the Li<sub>7</sub>La<sub>3</sub>Zr<sub>2</sub>O<sub>12</sub> Solid Electrolyte. *Chem. Mater.* **2018**, *30*, 3019–3027.
- (73) Jain, A.; Ong, S. P.; Hautier, G.; Chen, W.; Richards, W. D.; Dacek, S.; Cholia, S.; Gunter, D.; Skinner, D.; Ceder, G.; Persson, K. A. The Materials Project: A materials genome approach to accelerating materials innovation. *APL Mater.* **2013**, *1*, No. 011002.
- (74) Becke, A. D. Density-functional thermochemistry. III. The role of exact exchange. *J. Chem. Phys.* **1993**, *98*, 5648–5652.
- (75) Dion, M.; Rydberg, H.; Schröder, E.; Langreth, D. C.; Lundqvist, B. I. Van der Waals Density Functional for General Geometries. *Phys. Rev. Lett.* **2004**, *92*, No. 246401.
- (76) Taylor, J.; Guo, H.; Wang, J. Ab initio modeling of quantum transport properties of molecular electronic devices. *Phys. Rev. B* **2001**, *63*, No. 245407.
- (77) Mathew, K.; Sundararaman, R.; Letchworth-Weaver, K.; Arias, T. A.; Hennig, R. G. Implicit solvation model for density-functional study of nanocrystal surfaces and reaction pathways. *J. Chem. Phys.* **2014**, *140*, No. 084106.
- (78) Ringe, S.; Hörmann, N. G.; Oberhofer, H.; Reuter, K. Implicit Solvation Methods for Catalysis at Electrified Interfaces. *Chem. Rev.* **2022**, *122*, 10777–10820.